

Comet-type periodic motions and their out-of-plane bifurcations in the Earth–Moon CR3BP: a computational symplectic analysis

Cengiz Aydin

February 19, 2026

Abstract

Comet-type periodic orbits of the circular restricted three-body problem (CR3BP) are periodic solutions that are generated from very large retrograde and direct circular Keplerian motions around the common center of mass of the primaries. In this paper we first provide an analytical proof of the existence of comet-type periodic orbits by using the classical Poincaré continuation method. Within this analytical approach, we also determine their Conley–Zehnder index, defined as a Maslov index using a crossing form. Then, by applying a standard corrector–predictor technique, we explore numerically the two families of comet orbits within the Earth–Moon CR3BP. We compute their stability indices, identify vertical self-resonant orbits up to multiplicity six, investigate the vertically bifurcated periodic solutions and discuss their orbital characteristics. Our main results we illustrate in form of bifurcation graphs, based on symplectic invariants, which provide a topological overview of the connections of the bifurcated branches, including bridge families.

Keywords comet orbits · Earth–Moon CR3BP · Conley–Zehnder index · bifurcation graph
MSC 2020 70H12 · 70F07 · 70G45

Contents

1	Introduction	2
2	CR3BP dynamics	3
2.1	Equations of motion	3
2.2	Symmetries	5
2.3	Monodromy matrix and stability index	5
2.4	Out-of-plane bifurcations	7
3	Conley–Zehnder index	8
3.1	Transverse Conley–Zehnder index of a Hamiltonian orbit	8
3.2	Planar solutions, the case of $Sp(2)$ and index iteration	10
3.3	Interaction at bifurcation points	11
4	Analytical approach to comet-type periodic orbits	12
5	Numerical computational results within the Earth–Moon CR3BP	14
5.1	Retrograde and direct comet-type periodic orbits	15
5.2	Out-of-plane bifurcation results	17
6	Conclusion	24
Appendix	Tables of data	26

1 Introduction

One of the most promising problems in celestial mechanics is the search for periodic solutions of the Newtonian N -body problem, which describes the dynamics of N bodies of mass $m_i > 0$ ($i = 1, \dots, N$) moving and interacting according to Newton's law of gravitation. The equations of motion are given by

$$\ddot{r}_i = - \sum_{j=1, j \neq i}^N \frac{m_j(r_i - r_j)}{r_{ij}^3}, \quad 1 \leq i \leq N,$$

where the unit of time is chosen such that the gravitational constant is one, $r_i \in \mathbb{R}^3$ indicates the position of the i -body, and $r_{ij} = |r_i - r_j|$ denotes the Euclidean distance between the i -body and the j -body. While the 2-body problem has been completely understood [43], the N -body problem for $N \geq 3$ still remains without a general analytical solution [44]. A particular and simpler case of interest is the restricted problem which describes conveniently the dynamics of small bodies of the solar system. One assumes that one of the N bodies is significantly smaller than the other $N - 1$ bodies (called primaries) and thus has a negligible effect on their motion. Within this assumption, the motion of the primaries becomes a $(N - 1)$ -body problem to whose gravitational field the motion of the infinitesimal body is subject.

Among N -body systems, the 3-body problem is one of the most celebrated scenarios in each of astronomy, physics and mathematics. The circular restricted 3-body problem (CR3BP), in which the two primaries move in a circular fashion around their common center of mass, is used as a first approximation for the motion of a spacecraft in a Sun–planet or planet–moon environment. Periodic solutions of the CR3BP provide a paramount framework for the structure of all dynamically possible orbits and help to gain information on the stability and behavior of a given trajectory. In particular, space mission profiles and spacecraft trajectory designs associated to the renewed popularity of Lunar explorations, spurred by NASA's Cislunar mission Artemis [46], along with the Lunar Gateway [21], and Chang'e missions [27], demonstrate the crucial role of periodic orbits of the Earth–Moon CR3BP framework for operating orbits. Therefore, it becomes of vital importance to catalog as many periodic orbits as possible.

Although different kind of orbits of the Earth–Moon CR3BP have been widely studied [10, 15, 18, 47], there are still various types of periodic solutions that are sparsely explored in the literature, including comet-type periodic orbits and their out-of-plane bifurcations. Comet-type periodic orbits are periodic solutions that are generated from very large retrograde and direct circular Keplerian motions around the common center of mass of the primaries. Analytically, a first proof of their existence was given by Moulton [38] for the R3BP. Later, Meyer provided an existence proof for (restricted) N -body problems [33–35], which is extended in [29, 30] for a wider class of restricted N -body problems. More recently, [31] proved the existence of comet orbits within a special case of the CR4BP, and [14] analyzed them in an elliptic spatial restricted N -body problem. The technique of the existence proof is based on a common strategy [36]: for systems depending on a small parameter, a periodic solution of the unperturbed system exists in the perturbed system if its Floquet multipliers are different from the unity, as follows by the implicit function theorem. This small parameter method has its origin in Poincaré's pioneering work [40] which is therefore known as the Poincaré continuation method.

In classical works on numerical explorations, comet orbits and their planar linear stability behavior were investigated by Strömgren and his colleagues within the Copenhagen problem, a special case of the CR3BP when the two primaries have equal mass [45], by Broucke for the Earth–Moon CR3BP [10], and by Bruno for the Sun–Jupiter system [11, 12]. The corresponding orbit family notations are:

	CR3BP	direct comet orbits	retrograde comet orbits
Strömgren	Copenhagen problem	l	m
Broucke	Earth–Moon system	E_1	F
Bruno	Sun–Jupiter system	$ID - 1$	$IR -$

Out-of-plane bifurcations from comet orbits were analyzed in [25] for a gravitational model on the dynamics around the asteroid (433) Eros, and in [39] for a particular case of the CR4BP. For various CR3BP systems, [15] describes only partially some vertically bifurcated branches from retrograde comet orbits (labeled as family $C1$). Since we are not aware of more than the latter three articles on out-of-plane bifurcations from comet orbits, the present work aims at studying retrograde and direct comet periodic orbits and their vertical multiple-cover bifurcations, with a particular focus on the Earth–Moon environment. Throughout this paper, we denote the family of retrograde comet orbits by κ_- and the family of direct comet orbits by κ_+ .

In recent years, symplectic invariants (most significant is the Conley–Zehnder index) have been successfully applied to the numerical bifurcation analysis, leading to a topological overview of the global network structure and systematic classification of periodic orbit families [4–6, 22, 23, 26, 37]. This combination of symplectic methods and classical computational techniques also forms the key features in this work. Our results show that in almost all cases the bifurcated branches form bridge families. By a *bridge family* we understand a periodic orbit family between two different branch points, as defined in [28]. Therefore, bridge families are *closed families*, existing only on a finite interval of the energy values. Our vertical multiple-cover bifurcation results are:

- *Single-turn and period-doubling bifurcations from retrograde κ_- orbits.*

Solutions generated from single-turn bifurcation from κ_- correspond to L_1 halo orbits, and those computed from period-doubling bifurcation from κ_- agree with the families of L_2 and L_3 vertical Lyapunov orbits. We mention that these results are also described in [15], but are derived from solutions around the libration points.

- *Period-tripling bifurcation from retrograde κ_- orbit.*

Two bifurcated branches are obtained from period-tripling of κ_- orbits. While one branch forms a bridge family to a periodic solution which belongs to the family of retrograde solutions around the Earth (family $A1$ in Broucke’s notation), the other branch forms a bridge to single-turn bifurcation from a direct κ_+ orbit.

- *k -cover bifurcations from retrograde κ_- orbits ($k = 4, 5, 6$).*

Systematically, branches generated from k -covering of retrograde κ_- orbits form bridge families to $(k-2)$ -covering of direct κ_+ orbits, for $k = 4, 5, 6$.

- *Single-turn bifurcation from direct κ_+ orbit.*

From a single-turn branch point of κ_+ , we generate an orbit family whose members approach collision with the Earth. Most of the period the solutions are far from the Earth with a large excursion of hook-shaped form in the vertical direction, so that the near-collision phase is very brief. This kind of orbit is known within the CR3BP around the larger primary for small mass values, as bifurcation from vertical collision orbits in the rotating Kepler problem [7, 8].

Structure of the paper. In Section 2 we recall the CR3BP dynamics. The following Section 3 contains the construction of the Conley–Zehnder index and associated symplectic invariants. In Section 4 we provide an analytical approach to the comet orbits. We discuss an existence proof based on the Poincaré continuation method, and determine their Conley–Zehnder indices. In Section 5 we numerically explore the families of comet orbits and present the outcomes. We compute stability indices, identify vertical self-resonant orbits up to multiplicity six, analyze the vertically bifurcated branches and discuss their orbital characteristics. Main results, summarized briefly above, are illustrated in form of bifurcation graphs which provide a topological overview of the connections of the bifurcated branches, including bridge families. In Section 6 we summarize our work and conclude. Data base are collected in the Appendix.

2 CR3BP dynamics

2.1 Equations of motion

The spatial CR3BP refers to the dynamics of a body, of infinitesimal mass, that is subject to the gravitational field of two primary bodies moving along circles in the same plane with constant angular velocity

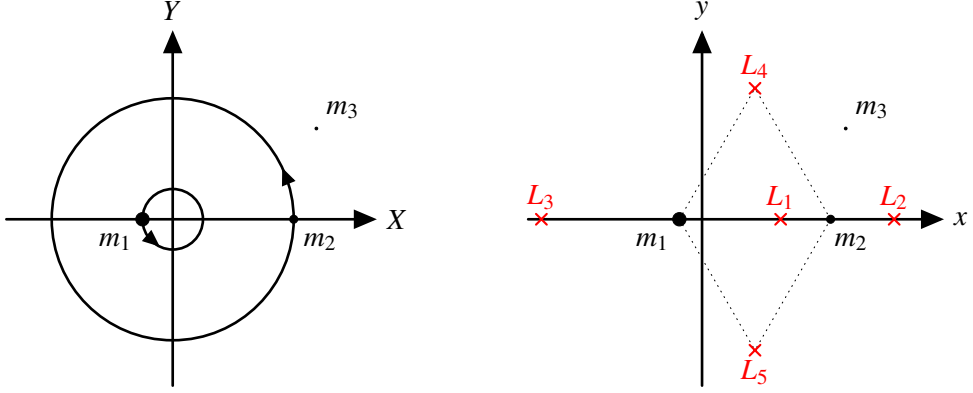


Figure 1: CR3BP in an inertial reference frame (X, Y) and in a rotating reference frame (x, y) , with primaries m_1 and m_2 , infinitesimal body m_3 and libration points L_i ($i = 1, 2, 3, 4, 5$).

around their common center of mass. The infinitesimal mass has a negligible effect on the motion of the primaries (see Figure 1). Taking a coordinate system that rotates with an angular velocity of the orbital angular rate of the primaries, and choosing suitable units, the primaries can be assumed to have masses $1 - \mu$ and μ with $\mu \in [0, \frac{1}{2}]$, to rest at the respective points $(-\mu, 0, 0)$ and $(1 - \mu, 0, 0)$, and to complete one inertial revolution in 2π time units. Within these assumptions, the motion of the infinitesimal body is governed by the second order differential equations [45, Chapter 1]:

$$\begin{aligned}\ddot{x} &= 2\dot{y} + x - (1 - \mu) \frac{x + \mu}{r_1^3} - \mu \frac{x - 1 + \mu}{r_2^3}, \\ \ddot{y} &= -2\dot{x} + y - \left(\frac{1 - \mu}{r_1^3} + \frac{\mu}{r_2^3} \right) y, \\ \ddot{z} &= - \left(\frac{1 - \mu}{r_1^3} + \frac{\mu}{r_2^3} \right) z,\end{aligned}\tag{1}$$

where $r_1 = ((x + \mu)^2 + y^2 + z^2)^{\frac{1}{2}}$ and $r_2 = ((x - 1 + \mu)^2 + y^2 + z^2)^{\frac{1}{2}}$ indicate the distances from the infinitesimal body to the primaries. The CR3BP framework has five points of equilibrium, also called libration points or Lagrange points [45, Chapter 4]: Three collinear points L_1 (located within the primaries), L_2 and L_3 (outside the interval joining the primaries), and two equilateral triangular points L_4 and L_5 , as shown in Figure 1.

Defining kinetic moments by

$$p_x = \dot{x} - y, \quad p_y = \dot{y} + x, \quad p_z = \dot{z},\tag{2}$$

the system can be written in Hamiltonian form with the corresponding Hamiltonian function

$$H(x, y, z, p_x, p_y, p_z) = \frac{1}{2} (p_x^2 + p_y^2 + p_z^2) - \frac{1 - \mu}{r_1} - \frac{\mu}{r_2} + p_x y - p_y x,\tag{3}$$

which is a first integral of the system. Thus, periodic solutions come in a smooth one-parameter family, parameterized by the energy. An equivalent first integral is the Jacobi constant $C = -2H$. The phase space of the system is 6-dimensional and endowed with the standard symplectic form $\omega_0 = \sum dp_k \wedge dk$ ($k = x, y, z$). The Hamiltonian vector field X_H , uniquely determined by $dH(\cdot) = \omega_0(\cdot, X_H)$, generates the Hamiltonian flow ϕ^t by the equations

$$\frac{d}{dt} \phi^t = X_H(\phi^t), \quad \phi^0 = \text{id},\tag{4}$$

which is equivalent to (1). In the linear algebra expression of ω_0 ,

$$\omega_0(\cdot, \cdot) = \langle J \cdot, \cdot \rangle, \quad \text{with } J = \begin{pmatrix} 0 & I_3 \\ -I_3 & 0 \end{pmatrix},$$

where the brackets denote the Euclidean inner product, we can represent the Hamiltonian vector field by

$$X_H = J\nabla H,$$

where the gradient, as usual, is defined with respect to the Euclidean inner product. With that, the equations (1) and (4) can be equivalently expressed by

$$\dot{\gamma} = J\nabla H(\gamma), \quad \gamma \equiv (x, y, z, p_x, p_y, p_z). \quad (5)$$

2.2 Symmetries

The Hamiltonian (3) is invariant under involutions on the phase space, called *symmetries*, given by:

$$OX := \rho_1(x, y, z, p_x, p_y, p_z) = (x, -y, -z, -p_x, p_y, p_z) \text{ } (\pi\text{-rotation around the } x\text{-axis}), \quad (6)$$

$$XOZ := \rho_2(x, y, z, p_x, p_y, p_z) = (x, -y, z, -p_x, p_y, -p_z) \text{ } (\text{reflection at the } xz\text{-plane}), \quad (7)$$

$$\sigma(x, y, z, p_x, p_y, p_z) = (x, y, -z, p_x, p_y, -p_z) \text{ } (\text{reflection at the ecliptic } \{z = 0\}). \quad (8)$$

Notice that $\rho_1 \circ \rho_2 = \rho_2 \circ \rho_1 = \sigma$. The planar problem corresponds to the restriction of the system to the fixed point set $\text{Fix}(\sigma) = \{(x, y, 0, p_x, p_y, 0)\}$, in which an inherent symmetry is characterized by $(x, y, 0, p_x, p_y, 0) \mapsto (x, -y, 0, -p_x, p_y, 0)$ (reflection at the x -axis). Moreover, while (8) is symplectic, (6) and (7) are anti-symplectic, which means that their matrix representations,

$$\begin{aligned} \Sigma_{OX} &= \text{diag}\{1, -1, -1, -1, 1, 1\}, \\ \Sigma_{XOZ} &= \text{diag}\{1, -1, 1, -1, 1, -1\}, \\ \Sigma_{\sigma} &= \text{diag}\{1, 1, -1, 1, 1, -1\}, \end{aligned}$$

satisfy $\Sigma_{\sigma} J \Sigma_{\sigma} = J$, and $\Sigma J \Sigma = -J$, where $\Sigma = \Sigma_{OX}$ or $\Sigma = \Sigma_{XOZ}$. While symplectic symmetries denote time-preserving symmetries, anti-symplectic symmetries denote time-reversal ones in the Hamiltonian context [24]. In the case of invariance under σ , the Hamiltonian flow ϕ^t satisfies

$$\sigma \circ \phi^t = \phi^t \circ \sigma, \quad (9)$$

and in the case of invariance under $\rho_{1/2}$, it holds that

$$\rho_i \circ \phi^{-t} = \phi^t \circ \rho_i, \quad \text{with } i \in 1, 2. \quad (10)$$

In particular, such invariant periodic orbits are divided into groups with different number of symmetries:

- *Simple symmetric w.r.t. OX-(or XOZ-)symmetry*: Orbit starts perpendicular at the x -axis (or xz -plane) and intersects the x -axis (or xz -plane) perpendicularly at half period.
- *Doubly symmetric w.r.t. OX-XOZ-(or XOZ-OX-)symmetry*: Orbit starts perpendicular at the x -axis (or xz -plane) and intersects the xz -plane (or x -axis) perpendicularly at quarter period.

2.3 Monodromy matrix and stability index

Let $\gamma \equiv (x, y, z, p_x, p_y, p_z)$ be a T -periodic solution of (5). Significant information on the orbit γ are provided by the linearized flow along γ , which represented by

$$d\phi^t =: V(t) = (v_{ij}) \in \mathbb{R}^{6 \times 6},$$

solves, in view of (5), the *variational equation*,

$$\dot{V}(t) = JD^2H(\gamma(t))V(t), \quad V(0) = \text{id}, \quad (11)$$

where D^2H is the Hessian of the Hamiltonian. Notice that $V(-t) = V^{-1}(t)$. The solution of (11) is also commonly called *state transition matrix* or *variational matrix*.

The *monodromy matrix* M of γ corresponds to the full period linearization, i.e., $M = V(T)$. Since the monodromy matrix is symplectic, which means that it satisfies $M^T JM = J$, or it is conjugate to a symplectic matrix by (2), the eigenvalues occur in reciprocal pairs and are of the form

$$\{1, 1, \lambda_1, \lambda_1^{-1}, \lambda_2, \lambda_2^{-1}\},$$

where 1 appears trivially twice since the energy is a first integral of the system. The non-trivial eigenvalues are called *Floquet multipliers*. The periodic orbit γ is *non-degenerate* when 1 is not among its Floquet multipliers. For each pair of Floquet multipliers the *stability index* is defined as

$$s_k = \frac{1}{2} (\lambda_k + \lambda_k^{-1}), \quad \text{for } k = 1, 2.$$

They can be of one of the following types:

- *Elliptic*: $-1 < s_k = \cos \theta < 1$. It is equivalent to $\lambda_k = e^{i\theta}$.
- *Positive hyperbolic*: $s_k > 1$. It is equivalent to $\lambda_k \in \mathbb{R}_{>0} \setminus \{1\}$.
- *Negative hyperbolic*: $s_k < -1$. It is equivalent to $\lambda_k \in \mathbb{R}_{<0} \setminus \{-1\}$.
- *Complex instability*: Case of quadruples $\{\lambda, \lambda^{-1}, \bar{\lambda}, \bar{\lambda}^{-1}\}$.

Stable periodic solutions are those that simultaneously satisfy $|s_1| < 1$ and $|s_2| < 1$. It is common to compute the stability indices via formulas, as given in the next lemma following [9].

Lemma 2.1. *The stability indices are determined by*

$$s_1 = -\frac{1}{4} (\alpha + \sqrt{\beta}), \quad s_2 = -\frac{1}{4} (\alpha - \sqrt{\beta}), \quad (12)$$

where $\alpha = 2 - \text{tr}(M)$, and $\beta = 2\text{tr}(M^2) - \alpha^2 + 4$.

Proof. The characteristic polynomial of M is of the form

$$\chi_M(\lambda) = (\lambda - 1)^2 (\lambda^4 + \alpha \lambda^3 + \beta' \lambda^2 + \alpha \lambda + 1),$$

where

$$\alpha = -\lambda_1 - \lambda_1^{-1} - \lambda_2 - \lambda_2^{-1}, \quad \beta' = \lambda_1 \lambda_2 + \lambda_1 \lambda_2^{-1} + \lambda_1^{-1} \lambda_2 + \lambda_1^{-1} \lambda_2^{-1} + 2.$$

The coefficients α and β' can also be written as

$$\alpha = 2 - \text{tr}(M), \quad \beta' = \frac{1}{2} \alpha^2 - \frac{1}{2} \text{tr}(M^2) + 1.$$

Taking into account the stability indices, an equivalent expression of $\chi_M(\lambda)$ is given by

$$\chi_M(\lambda) = (\lambda - 1)^2 (\lambda^4 + 2(-s_1 - s_2) \lambda^3 + (4s_1 s_2 + 2) \lambda^2 + 2(-s_1 - s_2) \lambda + 1).$$

Therefore, the stability indices satisfy the equations

$$-2(s_1 + s_2) = \alpha, \quad 4s_1 s_2 + 2 = \beta',$$

whose solutions correspond to (12). □

The next lemma shows that for symmetric periodic orbits, it is enough to linearize along the orbit from one symmetric point to the next symmetric point to obtain the monodromy matrix [9]. This in fact, offers economy of computing effort.

Lemma 2.2. *Let γ be a simple or doubly symmetric T -periodic orbit. Depending on the type of symmetries, the monodromy matrix of γ is determined as follows:*

- a) If γ is simple symmetric w.r.t. OX - or XOZ -symmetry, then correspondingly:

$$M = \Sigma_{OX}V^{-1}(T/2)\Sigma_{OX}V(T/2), \quad \text{or} \quad M = \Sigma_{XOZ}V^{-1}(T/2)\Sigma_{XOZ}V(T/2).$$

- b) If γ is doubly symmetric w.r.t. OX - XOZ - or XOZ - OX -symmetry, then correspondingly:

$$M = [\Sigma_{OX}V^{-1}(T/4)\Sigma_{XOZ}V(T/4)]^2, \quad \text{or} \quad M = [\Sigma_{XOZ}V^{-1}(T/4)\Sigma_{OX}V(T/4)]^2.$$

Proof. The proof for the respective second case in a) and b) is similar to that in the respective first cases, therefore it is sufficient to discuss only the corresponding first case. Let γ be simple symmetric w.r.t. OX -symmetry. Then, in view of the identity (10), the variational matrix satisfies

$$V^{-1}(t) = \Sigma_{OX}V(t)\Sigma_{OX}. \quad (13)$$

Equation (13) for $t = -T/2$, together with $V(T/2) = V^{-1}(T/2)V(T)$, becomes

$$V^{-1}(T/2)V(T) = \Sigma_{OX}V^{-1}(T/2)\Sigma_{OX},$$

which implies the first case in a). Now let γ be doubly symmetric w.r.t. OX - XOZ -symmetry. Since the orbit γ is symmetric w.r.t. OX -symmetry on half of its period, from the first case in a) we have that

$$M = \Sigma_{OX}V^{-1}(T/2)\Sigma_{OX}V(T/2). \quad (14)$$

Taking into account that $\Sigma_{OX}\Sigma_{XOZ} = \Sigma_{XOZ}\Sigma_{OX} = \Sigma_\sigma$, the variational matrix satisfies, in view of (9), that

$$V(t+T) = \Sigma_\sigma V(t)\Sigma_\sigma V(T). \quad (15)$$

The combination of (13) and (15) for $t = -T/4$ gives

$$V(T/2) = \Sigma_\sigma \Sigma_{OX}V^{-1}(T/4)\Sigma_{OX}\Sigma_\sigma V(T/4) = \Sigma_{XOZ}V^{-1}(T/4)\Sigma_{XOZ}V(T/4),$$

which, together with its inverse, inserted into (14) proves the first case in b). \square

Remark 2.3. In symplectic coordinates, the variational matrix $V(t)$ satisfies $V^T(t)JV(t) = J$, which means that in the formulas in Lemma 2.2, for the inverse one can use the identity $V^{-1}(t) = J^T V^T(t)J$.

2.4 Out-of-plane bifurcations

By virtue of the symplectic symmetry σ (8), planar periodic orbits have a planar and spatial stability index (also called horizontal or vertical stability index), which we denote correspondingly by s_p and s_v . The case $s_v = 1$ signals an out-of-plane bifurcation with spatial periodic orbits of the same period while the case $s_v = -1$ corresponds to a period-doubling bifurcation. *Vertical self-resonant* (VSR) orbits are those with Floquet multipliers equal to root of the unity, i.e., if the vertical stability index satisfies

$$s_v = \cos\left(2\pi\frac{d}{k}\right), \quad (16)$$

where $d, k \in \mathbb{Z}$ ($k \neq 1, 2$) with $d < k$ and d/k irreducible fraction. Such a critical orbit is also called *d:k resonant orbit*. As identified in [42], the k -covering with period kT generates bifurcation of exactly two spatial periodic orbit families whose symmetry properties depend on the multiplicity k :

- *Odd multiplicity k.* Members of the two new branches are simple symmetric; while orbits of one family are symmetric w.r.t. OX -symmetry, others are symmetric w.r.t. XOZ -symmetry.
- *Even multiplicity k.* Both new families consist of doubly symmetric periodic orbits; the orbits in one family are doubly symmetric w.r.t. OX - XOZ -symmetry, while those in the other are doubly symmetric w.r.t. XOZ - OX -symmetry.

3 Conley–Zehnder index

3.1 Transverse Conley–Zehnder index of a Hamiltonian orbit

An important invariant associated to Hamiltonian periodic solutions is the so-called Conley–Zehnder index [13]. Intuitively, it measures the winding number of the linearized flow along an orbit. Due to the time independence of the Hamiltonian framework we study, we consider the transverse Conley–Zehnder index of a periodic solution such as proposed in [1, 22, 23, 26, 37]. For our purpose, we look attentively at the approach in [1, 26] which is based on the Robbin–Salamon definition of the Maslov index using a crossing form [41]: Let $Sp(2n)$ denote the symplectic group, i.e.,

$$Sp(2n) = \{A \in \text{Mat}(2n, \mathbb{R}) : A^TJA = J\}, \quad \text{with } J = \begin{pmatrix} 0 & I_n \\ -I_n & 0 \end{pmatrix}.$$

Let $\Psi : [0, T] \rightarrow Sp(2n)$ be a path of symplectic matrices with $\Psi(0) = \text{id}$. A point t is called a **crossing** if $\ker(\Psi(t) - \text{id}) \neq 0$. For a crossing t the **crossing form** is defined as a quadratic form on the vector space $V_t = \ker(\Psi(t) - \text{id})$ by

$$Q_t(v, v) = \omega(v, \dot{\Psi}(t)v), \quad v \in V_t,$$

where ω is a symplectic form on V_t . Since in symplectic coordinates, ω is represented by the matrix

$$\Omega := \text{diag} \left\{ \begin{pmatrix} 0 & 1 \\ -1 & 0 \end{pmatrix}, \dots, \begin{pmatrix} 0 & 1 \\ -1 & 0 \end{pmatrix} \right\},$$

the crossing form can be expressed as a diagonal matrix by $Q_t = \Omega \Psi(t)$. Furthermore, the signature of the quadratic form is defined as $\text{sign}(Q_t) = n_+ - n_-$, where n_+ and n_- denote the counts of positive and negative entries, respectively. Assume that all crossings are isolated and non-degenerate, i.e., the crossing form Q_t at the crossing t is non-degenerate as a quadratic form. The **Maslov index** of Ψ (also called **Robbin–Salamon index**) is then defined as

$$\mu(\Psi) = \frac{1}{2} \text{sign}(Q_0) + \sum_{t \in (0, T) \text{ crossing}} \text{sign}(Q_t) + \frac{1}{2} \text{sign}(Q_T), \quad (17)$$

which has the following nice properties:

- 1) (*Homotopy*) Two paths of symplectic matrices are homotopic with end points fixed if and only if they have the same index.
- 2) (*Catenation*) If $\Psi : [a, b] \rightarrow Sp(2n)$ and $a < c < b$ then

$$\mu(\Psi) = \mu(\Psi|_{[a, c]}) + \mu(\Psi|_{[c, b]}).$$

- 3) (*Product*) Let $n = n' + n''$, and identify $Sp(2n') \times Sp(2n'')$ as a subgroup of $Sp(2n)$ in the obvious way. If Ψ', Ψ'' are paths in $Sp(2n')$, $Sp(2n'')$ respectively, then

$$\mu(\Psi' \oplus \Psi'') = \mu(\Psi') + \mu(\Psi''). \quad (18)$$

Now let H be a time-independent Hamiltonian on a phase space, say \mathbb{R}^{2n} , and let γ be a T -periodic orbit of the Hamiltonian vector field X_H . In order to relate the Maslov index to the orbit γ , we need a path of symplectic matrices, which in fact, is generated by the linearized flow along the orbit γ . We first have to fix a symplectic frame, or a symplectic trivialization, along the orbit γ . This frame consists of a symplectic basis of the tangent space at each point of the orbit γ , with respect to which we measure the winding of the linearized flow, as illustrated in Figure 2. The existence of such a symplectic trivialization is guaranteed by general theory [32, Chapter 2.6] within the assumption that the orbit γ is the boundary of a spanning disk in \mathbb{R}^{2n} .

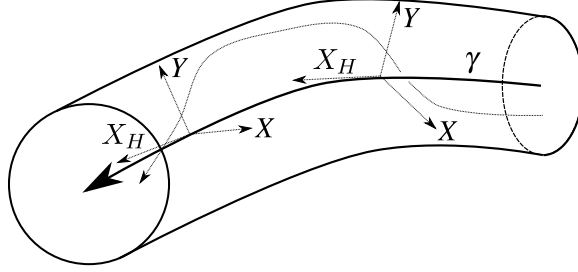


Figure 2: Conley–Zehnder index measures a twisting of the linearized flow along an orbit γ with respect to a frame.

Since the energy of the system is preserved, we first consider at each point of the periodic orbit γ a 2-dimensional symplectic vector space determined by

$$L := \langle Z, X_H \rangle, \quad \text{with } Z = \frac{1}{\|\nabla H\|^2} \nabla H.$$

The normalization of the vector Z ensures that $\omega(Z, X_H) = 1$. Therefore, $\{Z, X_H\}$ form a symplectic basis of the frame L . In order to generate a path of symplectic matrices induced by the linearized flow, we have to choose a symplectic basis $\{X_1, \dots, X_{n-1}, Y_1, \dots, Y_{n-1}\}$ of the $(2n-2)$ -dimensional symplectic complement of L , that is defined by

$$L^\omega = \{Y: \omega(X, Y) = 0 \text{ for } X \in L\}. \quad (19)$$

Such a symplectic basis can be achieved, for example, by the symplectic Gram–Schmidt process. In this way, on an energy level set $\Sigma = H^{-1}(c)$, $c \in \mathbb{R}$, at every point p of the orbit γ the symplectic basis of L^ω forms a $(2n-2)$ -dimensional frame that is transverse to the Hamiltonian vector field X_H . This frame determines a symplectic trivialization by

$$\Phi: \Sigma \times \mathbb{R}^{2n-2} \rightarrow L^\omega, \quad (p, u_1, \dots, u_{n-1}, v_1, \dots, v_{n-1}) \mapsto \sum_{i=1}^{n-1} u_i \cdot X_i(p) + \sum_{i=1}^{n-1} v_i \cdot Y_i(p).$$

Together with the projection map,

$$pr_{L^\omega}: T\mathbb{R}^{2n} \rightarrow L^\omega, \quad aZ + \sum_{i=1}^{n-1} u_i X_i + bX_H + \sum_{i=1}^{n-1} v_i Y_i \mapsto \sum_{i=1}^{n-1} u_i X_i + \sum_{i=1}^{n-1} v_i Y_i,$$

a path of symplectic matrices $\Psi_\gamma: [0, T] \rightarrow Sp(2n-2)$, that represents the transverse linearized flow, is now generated by

$$\Psi_\gamma(t) := (\Phi(\gamma(t), \cdot))^{-1} \circ pr_{L^\omega} \circ d\phi^t(\gamma(0)) \circ \Phi(\gamma(0), \cdot), \quad (20)$$

which is characterized by the diagram:

$$\begin{array}{ccc} \mathbb{R}^{2n-2} & \xrightarrow{\Psi_\gamma(t)} & \mathbb{R}^{2n-2} \\ \Phi(\gamma(0), \cdot) \downarrow & & \uparrow (\Phi(\gamma(t), \cdot))^{-1} \\ L^\omega_{\gamma(0)} & \xrightarrow{pr_{L^\omega} \circ d\phi^t(\gamma(0))} & L^\omega_{\gamma(t)} \end{array}$$

Then, the **transverse Conley–Zehnder index** of the orbit γ is defined as the Maslov index of the path Ψ_γ , denoted by

$$\mu_{CZ}(\gamma) := \mu(\Psi_\gamma),$$

which is invariant under continuous deformations of trivializations.

3.2 Planar solutions, the case of $Sp(2)$ and index iteration

Let now $\gamma \equiv (x, y, 0, p_x, p_y, 0)$ be a planar T -periodic solution of a spatial Hamiltonian system in which the planar system can be considered as the restriction of the system to the fixed point set of the symplectic symmetry σ (8), such as within the spatial CR3BP framework. Then, the 4-dimensional transverse frame associated to the planar orbit γ splits symplectically into 2-dimensional planar and spatial frames, which we denote correspondingly by $[X_p \ Y_p]$ and $[X_s \ Y_s]$. In this setting, a global trivialization can be chosen quite simply and explicitly: For the spatial frame, the out-of-plane directions,

$$X_s = \partial_{p_z}, \quad Y_s = \partial_z, \quad (21)$$

form a symplectic basis since $\omega(X_s, Y_s) = 1$. For the planar frame, it is convenient to work with quaternionic matrices [23, 37], which, restricted to planar variables, are given by

$$J = \begin{pmatrix} 0 & 0 & 1 & 0 \\ 0 & 0 & 0 & 1 \\ -1 & 0 & 0 & 0 \\ 0 & -1 & 0 & 0 \end{pmatrix}, \quad K_1 = \begin{pmatrix} 0 & 1 & 0 & 0 \\ -1 & 0 & 0 & 0 \\ 0 & 0 & 0 & -1 \\ 0 & 0 & 1 & 0 \end{pmatrix}, \quad K_2 = \begin{pmatrix} 0 & 0 & 0 & -1 \\ 0 & 0 & 1 & 0 \\ 0 & -1 & 0 & 0 \\ 1 & 0 & 0 & 0 \end{pmatrix}.$$

The vectors

$$X_p = \frac{1}{\|\nabla H\|} K_1 \nabla H, \quad Y_p = \frac{1}{\|\nabla H\|} K_2 \nabla H \quad (22)$$

satisfy $\omega(X_p, Y_p) = 1$, and form a symplectic basis to the symplectic complement (19), which is transverse to the Hamiltonian vector field $X_H = J \nabla H$ on an energy level set.

Furthermore, the path (20) decomposes symplectically into planar and spatial blocks:

$$\Psi_\gamma(t) = \begin{pmatrix} \Psi_\gamma^p(t) & 0 \\ 0 & \Psi_\gamma^s(t) \end{pmatrix}, \quad \Psi_\gamma^p(t), \Psi_\gamma^s(t): [0, T] \rightarrow Sp(2) = SL(2, \mathbb{R}).$$

In view of the product property of the Maslov index (18), the Conley–Zehnder index of the planar orbit γ splits additively into a planar and spatial index, which we denote by

$$\mu_{CZ}(\gamma) = \mu_{CZ}^p(\gamma) + \mu_{CZ}^s(\gamma).$$

If γ is non-degenerate, the definition of each index coincides with the construction by Hofer–Wysocki–Zehnder [20]: Let γ^k be the k -covering of γ and assume that γ^k is non-degenerate for all $k \geq 1$. The Conley–Zehnder index measures the rotation of corresponding eigenvectors, whose rotation angles are measured as a real number, and not modulo 2π , which is the case for rotation angles computed from monodromy matrices and Floquet multipliers. In the elliptic case, we denote by φ_p and φ_s the corresponding rotation angles as a real number for the underlying single-turn orbit γ . Then, each index is determined by

$$\mu_{CZ}^p(\gamma^k) = 1 + 2 \cdot \lfloor k \cdot \varphi_p / (2\pi) \rfloor, \quad \mu_{CZ}^s(\gamma^k) = 1 + 2 \cdot \lfloor k \cdot \varphi_s / (2\pi) \rfloor,$$

i.e., each index measures the number of times that eigenvalues crosses 1 along the whole orbit γ^k , jumping by 2 whenever 1 is crossed and being odd. It is worth to mention that in [3] we have used this Conley–Zehnder index construction to compute numerically the lunar periods that are known from astronomical observations.

In the hyperbolic case, the corresponding eigenvectors are rotated by $n\pi$ for an integer n , and the corresponding index equals

$$\mu_{CZ}^{p/s}(\gamma^k) = kn, \quad n \in \begin{cases} 2\mathbb{Z} & \text{for the pos. hyperbolic case} \\ 2\mathbb{Z} + 1 & \text{for the neg. hyperbolic case.} \end{cases}$$

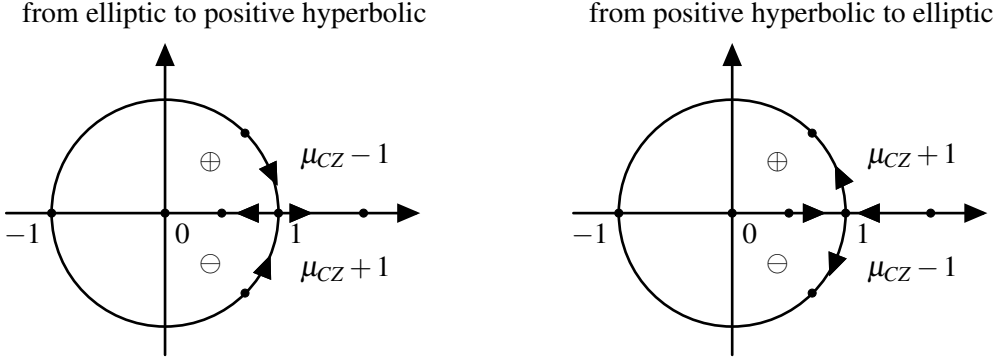


Figure 3: The index jump. Left: When eigenvalue 1 is crossed from above (or below), the index goes down (or up) by 1. Right: When Floquet multipliers after crossing eigenvalue 1 goes up (or down), the index goes up (or down) by 1. Direction of crossing is determined by \pm Krein signature.

3.3 Interaction at bifurcation points

Along the continuation of an orbit family, when reaching a bifurcation point within a transition from elliptic to positive hyperbolic, or vice versa, the corresponding index jumps by ± 1 , according to direction of crossing the eigenvalue 1, as shown in Figure 3. When there is a touching of the eigenvalue 1, the index jumps by ± 2 , determined by direction of rotation angles. In order to determine this direction of rotation, we consider the **Krein signature** [2, Appendix 29] which relates a \pm sign to each pair of elliptic Floquet multipliers: Let $M \in Sp(2n)$, and let $\{\lambda, \bar{\lambda}\}$ be a pair of elliptic eigenvalues of M of the form $\lambda = e^{i\theta}$, $\bar{\lambda} = e^{-i\theta}$ with $\lambda \bar{\lambda} \neq 1$. On the real 2-dimensional plane $P := \langle \text{Re}(v), \text{Im}(v) \rangle$, where v is an eigenvector of M with eigenvalue λ , a quadratic form is defined by

$$Q(\xi, \xi) := \omega(\xi, M\xi), \quad \xi \in P, \quad (23)$$

which in matrix form is represented by

$$Q = B^T J^T M B, \quad (24)$$

with $B = [\text{Re}(v) \ \text{Im}(v)] \in \text{Mat}(2n \times 2, \mathbb{R})$. This quadratic form is non-degenerate, either positive or negative definite. The **Krein signature** associated to the elliptic pair $\{\lambda, \bar{\lambda}\}$ is defined as the signature of the quadratic form Q , which is a symplectic invariant due to its independent choice of the eigenvector. In particular, if the signature is positive then the rotation is determined by $\theta \in (0, \pi)$, and if the signature is negative then the rotation is determined by $-\theta$ in the range $(\pi, 2\pi)$. Krein's main result was that collision of two pairs of elliptic Floquet multipliers with different signatures on the unit circle can provoke complex instability, while collision with same signatures does not cause a move off the unit circle. For our purpose, we use the Krein signature to specify the index jump, as illustrated in Figure 3. Moreover, for VSR orbits we derive from the Krein signature the concrete value of the integer d in (16).

When working locally near a family of non-degenerate periodic orbits, then there is a fascinating topological bifurcation invariant, based on holomorphic curves [19]: the **local Floer homology** and its **Euler characteristic**, the alternating sum of the ranks of the homology groups. Generators are periodic orbits, and significantly, the index leads to a grading on local homology groups. Therefore, the index provides important information how different families are related to each other at branch points. In our computations, it is crucial to check the invariance of the Euler characteristic by counting periodic orbits with indices locally at bifurcation points. Furthermore, in the sense of SFT [16], for planar orbits γ , if

$$\mu_{CZ}^p(\gamma^k) \equiv \mu_{CZ}^p(\gamma) \pmod{2}, \quad \mu_{CZ}^s(\gamma^k) \equiv \mu_{CZ}^s(\gamma) \pmod{2}, \quad (25)$$

or both equations in (25) are not simultaneously satisfied, then γ^k is called *good orbit*. Otherwise, γ^k is called *bad orbit* that are ignored in the local Floer homology. Therefore, locally at branch points

only good orbits will be counted with indices. Notice that all single-turn periodic orbits are good, and bad orbits occur as k -covering of orbits whose exactly one pair of Floquet multipliers is of negative hyperbolic type, where k is even. For spatial solutions, we treat each pair of Floquet multipliers and its interactions with Conley–Zehnder indices at bifurcation points in the same way as described before.

4 Analytical approach to comet-type periodic orbits

In this section we now study analytically two one-parameter families of planar nearly circular periodic orbits of the CR3BP which are located far away from the common center of mass of the primaries. These solutions are called *comet-type periodic orbits*. We first prove their existence by using a classical procedure, the Poincaré continuation method, such as proposed in [36, Chapter 9]. Then, we determine their Conley–Zehnder indices by applying the construction from the previous section. Results in this section hold for all mass ratios $\mu \in (0, \frac{1}{2}]$ of the CR3BP.

Theorem 4.1. *There exist two one-parameter families of planar nearly circular periodic orbits of the CR3BP which are at a great distance from the common center of mass of the primaries. One family exists for low Jacobi constants whose members we denote by κ_- , and orbits of the other family exist for high Jacobi constants which we denote by κ_+ . Moreover, orbits of both families are of elliptic type, their Conley–Zehnder indices are given by*

$$\mu_{CZ}(\kappa_{\pm}) = \mu_{CZ}^p(\kappa_{\pm}) + \mu_{CZ}^s(\kappa_{\pm}) = 2 = 1 + 1, \quad (26)$$

and they have both positive planar and spatial Krein signatures.

Periodic solutions that are associated to κ_+ we refer to as *direct/prograde comet-type periodic orbits*, and those that are related to κ_- we refer to as *retrograde comet-type periodic orbits*. Before we prove Theorem 4.1, we first discuss in the next theorem the Hamiltonian (3) of the CR3BP when we introduce a small scale parameter ε to approximate such comet orbits with very large radii.

Theorem 4.2. *Let $\varepsilon > 0$ be a small parameter. After the conformally symplectic scaling*

$$(x, y, z, p_x, p_y, p_z) \mapsto (\varepsilon^{-2}x, \varepsilon^{-2}y, \varepsilon^{-2}z, \varepsilon p_x, \varepsilon p_y, \varepsilon p_z), \quad (27)$$

the Hamiltonian of the CR3BP (3) becomes

$$H = p_{xy} - p_{yx} + \varepsilon^3 \left(\frac{1}{2} (p_x^2 + p_y^2 + p_z^2) - \frac{1}{(x^2 + y^2 + z^2)^{1/2}} \right) + O(\varepsilon^5). \quad (28)$$

From (28) we observe that when ε is very small, which in view of the scaling (27) means that the infinitesimal body is at a great distance from the primaries, the dominating force is the Coriolis force, and the next most significant force looks like a Kepler problem with both point masses at the origin.

Proof of Theorem 4.2. We first note that the scaling (27) is conformally symplectic with constant conformal factor ε^{-1} . To incorporate this magnification we consider a transformation of the Hamiltonian (3) given by $H \rightarrow \varepsilon H (\varepsilon^{-2}x, \varepsilon^{-2}y, \varepsilon^{-2}z, \varepsilon p_x, \varepsilon p_y, \varepsilon p_z)$, which reads

$$p_{xy} - p_{yx} + \frac{1}{2} \varepsilon^3 (p_x^2 + p_y^2 + p_z^2) - \varepsilon (U_1^\varepsilon(x, y, z) + U_2^\varepsilon(x, y, z)), \quad (29)$$

where

$$U_1^\varepsilon(x, y, z) = \frac{1 - \mu}{(\tilde{r} + \mu^2 + 2\mu x/\varepsilon^2)^{1/2}}, \quad U_2^\varepsilon(x, y, z) = \frac{\mu}{(\tilde{r} + (1 - \mu)^2 - 2(1 - \mu)x/\varepsilon^2)^{1/2}}, \quad (30)$$

and $\tilde{r} := (x^2 + y^2 + z^2)/\varepsilon^4$. We next simplify (30) by Legendre expansions. To this end, we write

$$U_1^\varepsilon(x, y, z) = \varepsilon^2 \frac{1 - \mu}{r(1 - 2\mathbf{x}\mathbf{t} + \mathbf{t}^2)^{1/2}}, \quad U_2^\varepsilon(x, y, z) = \varepsilon^2 \frac{\mu}{r(1 - 2\tilde{\mathbf{x}}\tilde{\mathbf{t}} + \tilde{\mathbf{t}}^2)^{1/2}}, \quad (31)$$

where

$$\mathbf{x} = -x/r, \quad \mathbf{t} = \varepsilon^2 \mu / r, \quad \tilde{\mathbf{x}} = x/r, \quad \tilde{\mathbf{t}} = \varepsilon^2 (1 - \mu) / r, \quad r = (x^2 + y^2 + z^2)^{1/2}. \quad (32)$$

Since $|\mathbf{x}| < 1$ and $|\tilde{\mathbf{x}}| < 1$, the corresponding expansions of (31) in terms of Legendre polynomials are given by

$$U_1^\varepsilon(x, y, z) = \varepsilon^2 \frac{1 - \mu}{r} \sum_{n=0}^{\infty} P_n(\mathbf{x}) \mathbf{t}^n, \quad P_0(\mathbf{x}) = 1, \quad P_1(\mathbf{x}) = \mathbf{x}, \quad (33)$$

and

$$U_2^\varepsilon(x, y, z) = \varepsilon^2 \frac{\mu}{r} \sum_{m=0}^{\infty} P_m(\tilde{\mathbf{x}}) \tilde{\mathbf{t}}^m, \quad P_0(\tilde{\mathbf{x}}) = 1, \quad P_1(\tilde{\mathbf{x}}) = \tilde{\mathbf{x}}. \quad (34)$$

By using the expressions (33) and (34), together with (32), we obtain

$$U_1^\varepsilon(x, y, z) + U_2^\varepsilon(x, y, z) = \varepsilon^2 \left(\frac{1}{r} - \frac{x(1 - 2\mu)}{r^2} + \frac{1 - \mu}{r} \sum_{n=2}^{\infty} P_n(\mathbf{x}) \mathbf{t}^n + \frac{\mu}{r} \sum_{m=2}^{\infty} P_m(\tilde{\mathbf{x}}) \tilde{\mathbf{t}}^m \right),$$

which, when inserted into (29), proves the theorem. \square

Proof of Theorem 4.1. In cylindrical symplectic coordinates $(r, \theta, z, p_r, p_\theta, p_z)$, introduced as follows,

$$\begin{aligned} x &= r \cos \theta, & p_x &= p_r \cos \theta - \frac{p_\theta}{r} \sin \theta, \\ y &= r \sin \theta, & p_y &= p_r \sin \theta + \frac{p_\theta}{r} \cos \theta, \\ z &= z, & p_z &= p_z, \end{aligned}$$

the Hamiltonian (28) becomes

$$H = -p_\theta + \varepsilon^3 \left(\frac{1}{2} (p_r^2 + p_\theta^2/r^2 + p_z^2) - \frac{1}{(r^2 + z^2)^{1/2}} \right) + O(\varepsilon^5). \quad (35)$$

The equations of motion are given by

$$\begin{aligned} \dot{r} &= \varepsilon^3 p_r, & \dot{p}_r &= \varepsilon^3 \left(\frac{p_\theta^2}{r^3} - \frac{r}{(r^2 + z^2)^{3/2}} \right), \\ \dot{\theta} &= \varepsilon^3 \frac{p_\theta}{r^2} - 1, & \dot{p}_\theta &= 0, \\ \dot{z} &= \varepsilon^3 p_z, & \dot{p}_z &= -\varepsilon^3 \frac{z}{(r^2 + z^2)^{3/2}}, \end{aligned} \quad (36)$$

where the terms of order ε^5 have been omitted. Within this order of approximation, p_θ is an integral. We shall now look for circular periodic solutions of (36) on the ecliptic $\{z = p_z = 0\}$. We find that the system (36) accepts a pair of circular periodic solutions determined by

$$r = 1, \quad p_r = 0, \quad p_\theta = \pm 1, \quad (37)$$

which are periodic of period $T = 2\pi/(1 \mp \varepsilon^3)$. In order to linearize the equations (36) near the circular solutions (37), we expand $(r + \Delta r, \theta + \Delta\theta, z + \Delta z, p_r + \Delta p_r, p_\theta + \Delta p_\theta, p_z + \Delta p_z)$ near (37), which leads to the autonomous linearized equations split into 4 dimensional planar and 2 dimensional spatial components:

$$\begin{pmatrix} \Delta \dot{r} \\ \Delta \dot{\theta} \\ \Delta \dot{p}_r \\ \Delta \dot{p}_\theta \end{pmatrix} = \begin{pmatrix} 0 & 0 & \varepsilon^3 & 0 \\ \mp 2\varepsilon^3 & 0 & 0 & \varepsilon^3 \\ -\varepsilon^3 & 0 & 0 & \pm 2\varepsilon^3 \\ 0 & 0 & 0 & 0 \end{pmatrix} \begin{pmatrix} \Delta r \\ \Delta \theta \\ \Delta p_r \\ \Delta p_\theta \end{pmatrix}, \quad \begin{pmatrix} \Delta \dot{z} \\ \Delta \dot{p}_z \end{pmatrix} = \begin{pmatrix} 0 & \varepsilon^3 \\ -\varepsilon^3 & 0 \end{pmatrix} \begin{pmatrix} \Delta z \\ \Delta p_z \end{pmatrix}. \quad (38)$$

The Jordan normal form of corresponding matrix exponential is given by

$$\text{diag} \left\{ \begin{pmatrix} 1 & 1 \\ 0 & 1 \end{pmatrix}, \begin{pmatrix} e^{i\epsilon^3 t} & 0 \\ 0 & e^{-i\epsilon^3 t} \end{pmatrix} \right\}, \quad \begin{pmatrix} e^{i\epsilon^3 t} & 0 \\ 0 & e^{-i\epsilon^3 t} \end{pmatrix}.$$

Notice that the top-left 2×2 -block appears since when the energy (or period) varies, the period (or energy) varies as well. Moreover, at the first return time $T = 2\pi/(1 \mp \epsilon^3)$ we obtain the planar and spatial Floquet multipliers, both of which are of the form

$$e^{\pm i\epsilon^3 2\pi/(1 \mp \epsilon^3)} = 1 \pm \epsilon^3 2\pi i + O(\epsilon^6). \quad (39)$$

With respect to the planar Floquet multipliers, by using the Poincaré continuation method [36, Chapter 9], we conclude that the two solutions (37) of the equations (36) can be continued to the full equations related to (35), where the $O(\epsilon^5)$ terms are included. This proves the assertion on the existence in the theorem. We denote by κ_+ the periodic solutions that are associated to $p_\theta = 1$, and by κ_- those that are related to $p_\theta = -1$. For the computation of their Conley–Zehnder indices, we first note that the Hamiltonian vector field at the solutions (37) is of the form $X_H = (\pm \epsilon^3 - 1)\partial_\theta$. Taking into account the trivializations (22) and (21), the planar and spatial frames, $[X_p, Y_p]$ and $[X_s, Y_s]$, are formed by the vectors

$$X_p = \partial_{p_r}, \quad Y_p = \partial_r, \quad X_s = \partial_{p_z}, \quad Y_s = \partial_z.$$

In view of (38), the transverse linearized flow with respect to these frames is given by

$$\text{diag} \left\{ \begin{pmatrix} 0 & -\epsilon^3 \\ \epsilon^3 & 0 \end{pmatrix}, \begin{pmatrix} 0 & -\epsilon^3 \\ \epsilon^3 & 0 \end{pmatrix} \right\},$$

whose matrix exponential provides a path of symplectic matrices,

$$\Psi_{\kappa_\pm}(t) = \begin{pmatrix} \Psi_{\kappa_\pm}^p(t) & 0 \\ 0 & \Psi_{\kappa_\pm}^s(t) \end{pmatrix} = \begin{pmatrix} \cos(t\epsilon^3) & -\sin(t\epsilon^3) & 0 & 0 \\ \sin(t\epsilon^3) & \cos(t\epsilon^3) & 0 & 0 \\ 0 & 0 & \cos(t\epsilon^3) & -\sin(t\epsilon^3) \\ 0 & 0 & \sin(t\epsilon^3) & \cos(t\epsilon^3) \end{pmatrix}, \quad (40)$$

which has crossings at $t \in 2\pi\mathbb{Z}/\epsilon^3$. Furthermore, the crossing form,

$$Q_t = \begin{pmatrix} 0 & 1 & 0 & 0 \\ -1 & 0 & 0 & 0 \\ 0 & 0 & 0 & 1 \\ 0 & 0 & -1 & 0 \end{pmatrix} \Psi_{\kappa_\pm}(t) = \begin{pmatrix} \epsilon^3 & 0 & 0 & 0 \\ 0 & \epsilon^3 & 0 & 0 \\ 0 & 0 & \epsilon^3 & 0 \\ 0 & 0 & 0 & \epsilon^3 \end{pmatrix},$$

has always planar and spatial signature 2. We observe that the path (40) rotates extremely slowly with a very large period of $2\pi/\epsilon^3$. It is evident that during one period of the solutions (37) there is no crossing, which, in view of the definition of the Maslov index (17), proves the Conley–Zehnder indices as stated in (26). Furthermore, eigenvectors to the Floquet multipliers (39) are of the form $[\pm i \ 1]^T$. By using (24), it is now a straightforward computation that on the plane $P = \langle [0 \ 1]^T, [1 \ 0]^T \rangle$ the quadratic form (23) is positive definite, which means that the orbits κ_\pm have planar and spatial positive Krein signatures. \square

5 Numerical computational results within the Earth–Moon CR3BP

For the results in this section, we have performed numerical integration of the equations of motion (1) and its variations (11) by using an explicit Runge–Kutta method of order twelve, such as proposed in [17], which we have encoded in Python. All periodic solutions have been obtained via a classical corrector–predictor continuation method [42] and computed within an accuracy of 10^{-8} . The mass ratio assumed for the Earth–Moon environment is $\mu = 1/82.27 \approx 0.0121550991$.

5.1 Retrograde and direct comet-type periodic orbits

For the numerical exploration of comet orbits we start with a first decent initial guess provided by large circular Keplerian motions centered at the origin. The initial data of planar circular periodic solutions within the rotating Kepler problem, which is a special case of the CR3BP when $\mu = 0$, are of the form

$$(x_0, 0, 0, 0, \dot{y}_0, 0), \quad \dot{y}_0 = \pm \frac{1}{\sqrt{x_0}} - x_0, \quad (41)$$

where $x_0 > 0$ is the Keplerian semi-major axis and \pm indicates the respective direct and retrograde motion. The corresponding energy value equals $-1/(2x_0) \mp \sqrt{x_0}$. For large semi-major axis x_0 , these orbits have the following properties:

- the Keplerian period equals $T_{\pm} = 2\pi/(1 \mp x_0^{-3/2})$ which is slightly above 2π for the direct, and slightly below 2π for the retrograde orbits;
- the energy values are very low for the direct and very high for the retrograde orbits; and
- while the retrograde orbits are retrograde in both the rotating and inertial frame, the direct orbits are direct in the inertial and retrograde in the rotating frame.

Moreover, these solutions are simple symmetric with only two perpendicular intersections with the x -axis per period. Therefore, by choosing an initial guess of the form (41) and integrating the equations of motion (1), the symmetric orbit will be periodic if at $t = T/2$ it fulfills the periodicity conditions:

$$y(x_0, 0, 0, 0, \dot{y}_0, 0) = 0, \quad \dot{x}(x_0, 0, 0, 0, \dot{y}_0, 0) = 0. \quad (42)$$

Since these conditions are only approximately satisfied, we seek appropriate corrections $\delta x_0, \delta \dot{y}_0, \delta t$ to fulfill these conditions with a specified accuracy. For this purpose we consider the first-order Taylor expansion of (42) and obtain

$$\begin{aligned} y + v_{21}\delta x_0 + v_{25}\delta \dot{y}_0 + \dot{y}(t)\delta t &= 0, \\ \dot{x} + v_{41}\delta x_0 + v_{45}\delta \dot{y}_0 + \ddot{x}(t)\delta t &= 0, \end{aligned} \quad (43)$$

where $v_{21} = \partial y / \partial x_0$, $v_{25} = \partial y / \partial \dot{y}_0$, $v_{41} = \partial \dot{x} / \partial x_0$ and $v_{45} = \partial \dot{x} / \partial \dot{y}_0$ are corresponding entries of the variational matrix $V(t) = (v_{ij}) \in \mathbb{R}^{6 \times 6}$ determined by (11). By fixing one of the three unknowns in (43), we solve (43) for the remaining two, and start a new integration of the equations (1) with the corrected initial data. We repeat the procedure in an iterative way of correction steps until a specified accuracy is satisfied. When a symmetric periodic orbit has been determined, we consider an arbitrary step of the initial parameter that we have fixed in the corrector steps, and obtain for the continuation the predictor scheme as previously. The choice of which of the parameters to fix has an important effect on the convergence of the solutions. If the fixed parameter reaches an extremum, the algorithm will break off and a new choice has to be considered.

Using the above corrector-predictor algorithm we have computed the two families κ_{\pm} of direct and retrograde comet-type periodic orbits. In Figure 4 and in Figure 5 we present periodic orbit plots for certain Jacobi constant values, and also show the planar and vertical stability diagrams. Vertical self-resonant (VSR) orbits are also identified which we denote in the form $d:k$ with respect to the vertical stability index in the elliptic case when $s_v = \cos(2\pi d/k)$. The data base are collected in Table A1.

Retrograde κ_- orbits. Along the continuation of the retrograde comet solutions, the orbit's geometry shape changes smoothly from the circular type to an ellipse-type orbit around both primaries, as shown in Figure 4. The Jacobi constant values increase, reach a maximum at $C \approx -0.412925$ (corresponding to a birth-death or saddle-node bifurcation; that is a branch point from which two families bifurcate into the same energy direction with an index difference of 1), and decrease further to very low values. At the limit, there is a rectilinear orbit between both primaries with infinite velocity and infinite energy [10].

We recall from Theorem 4.1 that the orbits start being elliptic with positive Krein signature and Conley-Zehnder index

$$\mu_{CZ}(\kappa_-) = 2 = \mu_{CZ}^p(\kappa_-) + \mu_{CZ}^s(\kappa_-) = 1 + 1.$$

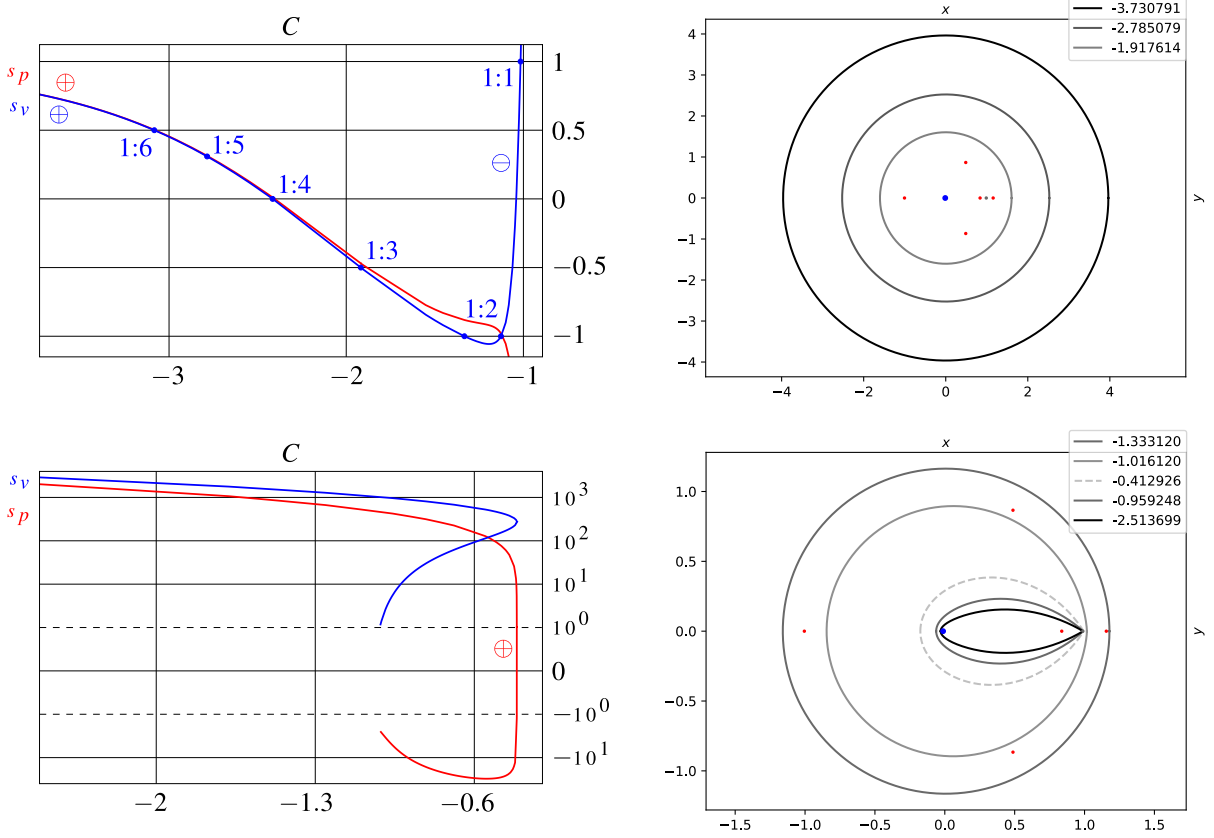


Figure 4: Family κ_- of retrograde comet-type periodic orbits. Right top shows κ_- orbits starting at low Jacobi constants; from dark to light (or from light to dark) indicates decreasing (or increasing) of energy values. Right bottom shows continuation of κ_- orbits; grey dashed is an orbit of birth-death type. Left top shows planar and vertical stability diagrams, s_p and s_v , continued left bottom where a logarithmic scale is used. In the elliptic range at left top, $d:k$ VSR orbits are denoted with respect to $s_v = \cos(2\pi d/k)$. \pm sign indicates Krein signature.

As can be observed in the stability diagrams in Figure 4, both of the planar and vertical stability indices, s_p and s_v , decrease, whereby s_v is slightly below s_p . At the Jacobi constant value $C \approx -1.333119$ the vertical stability index s_v crosses -1 , and after a short negative hyperbolic phase it becomes elliptic again at $C \approx -1.126762$, with negative Krein signature. After that, the vertical index increases extremely rapidly, crosses $+1$ at $C \approx -1.016119$ and becomes positive hyperbolic, and grows strongly in the positive hyperbolic direction. At the latter transition, due to the negative Krein signature, the spatial Conley–Zehnder index jumps from 1 to 2 . On the vertical stability diagram in Figure 4 we have identified the first occurring VSR orbits up to multiplicity six with respect to the vertical stability index, denoted by $1:6$, $1:5$, $1:4$, $1:3$, $1:2$ (two times) and $1:1$, as shown in Figure 4. Initial data are listed in Table A1. Shortly after the vertical stability index s_v crosses -1 the second time (transition of s_v from negative hyperbolic to elliptic), the planar stability index s_p also crosses -1 . After that, s_p remains negative hyperbolic for a while, increases very quickly, becomes elliptic with positive Krein signature, crosses $+1$ corresponding to birth-death bifurcation, and increases further in the positive hyperbolic way, moving closely below the vertical stability index. At the birth-death branch point, since the Krein signature is positive, the planar Conley–Zehnder index jumps from 1 to 0 .

Direct κ_+ orbits. Generated for high Jacobi constant values, the continuation of this family is in the decreasing direction of the Jacobi constant. As shown in Figure 5, a symmetric point on the trajectory moves closer to the libration point L_3 and forces a loop, such that the trajectories only intersect the x -axis perpendicularly when they cross it for the second time. This loop then evolves into a collision with the Earth, where we stop the continuation. Same as for the retrograde comet orbits, we know

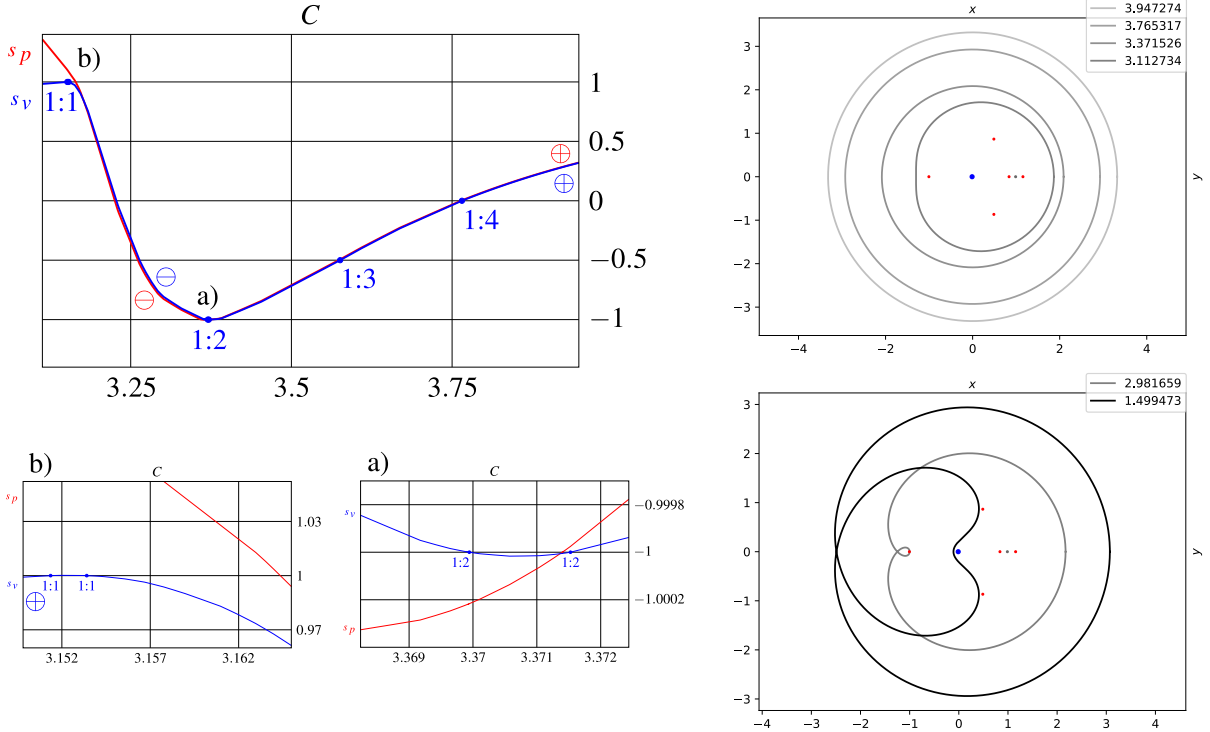


Figure 5: Family κ_+ of direct comet-type periodic orbits, continued up to approaching collision with the Earth. Right top shows κ_+ orbits starting at high Jacobi constants; from light to dark indicates increasing of energy values. Right bottom shows continuation of κ_+ orbits. Left top shows planar and vertical stability diagrams, s_p and s_v . Left bottom shows zoomed regions, a) with respect to crossing of -1 , and b) with respect to crossing of 1 . In the elliptic range at left top, $d:k$ VSR orbits are denoted with respect to $s_v = \cos(2\pi d/k)$. \pm sign indicates Krein signature.

from Theorem 4.1 that the direct comet orbits also start being elliptic with positive Krein signature and Conley–Zehnder index

$$\mu_{CZ}(\kappa_+) = 2 = \mu_{CZ}^p(\kappa_+) + \mu_{CZ}^s(\kappa_+) = 1 + 1.$$

As depicted in Figure 5, the planar and vertical stability indices behave similarly, with the planar index being slightly above the vertical index. Both decrease, become negative hyperbolic for a very short phase, and then become elliptic again with negative Krein signature. After that, both stability indices cross $+1$, and at this transition, since the Krein signatures are negative, both Conley–Zehnder indices jump from 1 to 2. Then, the planar stability index remains positive hyperbolic, and the vertical stability index, after a very short time in the positive hyperbolic region, becomes elliptic again with positive Krein signature, where the spatial Conley–Zehnder index jumps from 2 to 3. In order to make the very short negative and positive hyperbolic phases more visible, as shown in Figure 5, we had to work with very small step sizes in the corrector–predictor algorithm (43). Furthermore, with respect to the vertical stability diagram in Figure 5, we have identified VSR orbits up to multiplicity four, denoted by 1:4, 1:3, 1:2 (two times) and 1:1 (two times).

5.2 Out-of-plane bifurcation results

By adapting the corrector–predictor method (43) for spatial solutions, together with the computational technique of Conley–Zehnder index from Section 3, we have analyzed all vertical bifurcations that emanate from the VSR orbits identified above. We illustrate our main results in form of bifurcation graphs that provide a topological perspective, constructed in the following way. Vertices are branch points and edges are orbit families, labeled with Conley–Zehnder index. We draw from bottom to top in the direction of decreasing the Jacobi constant. Bold Jacobi constants correspond to critical branch points. Thick

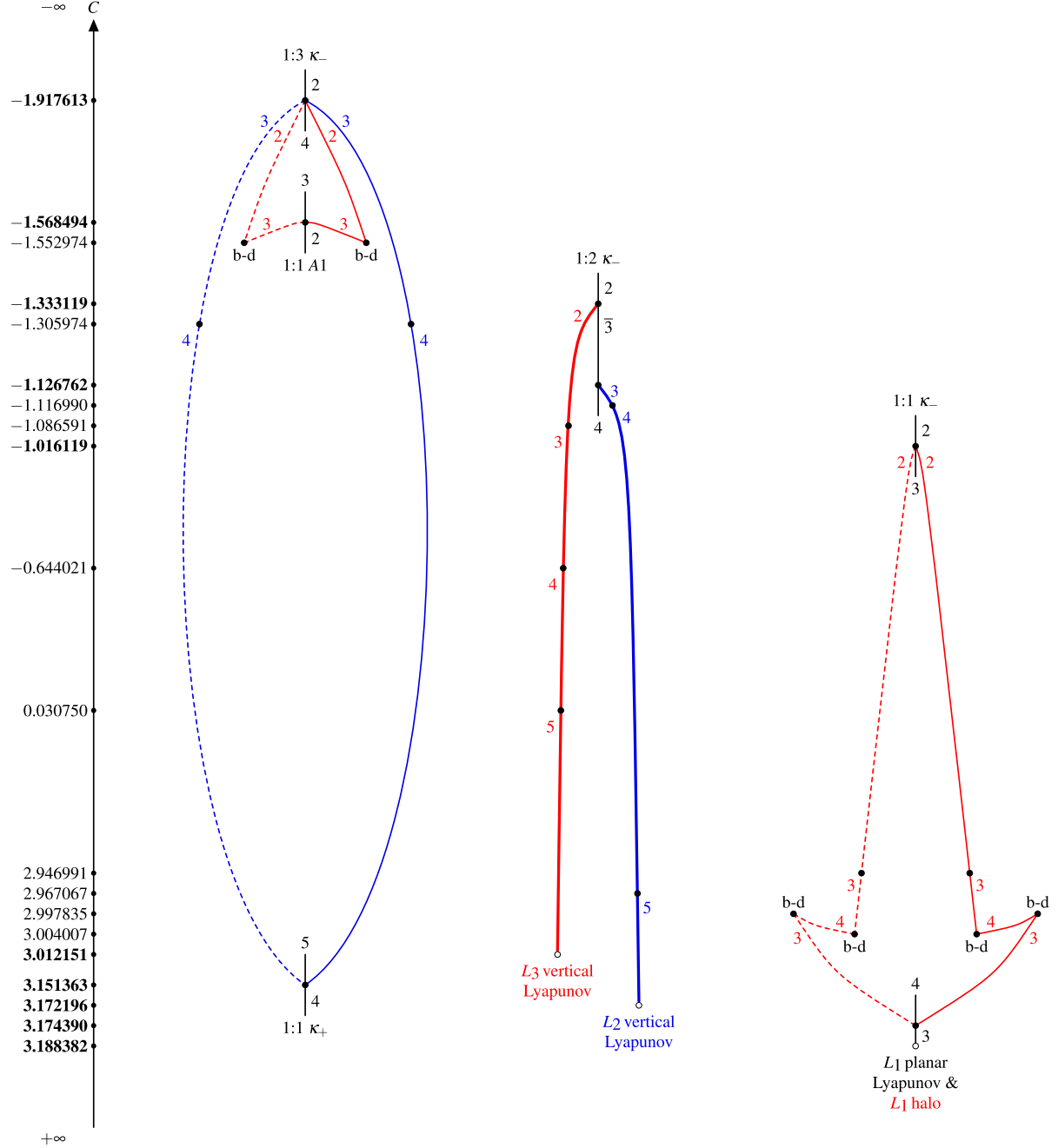


Figure 6: Bifurcation diagram associated to vertically bifurcated branches from $1:1 \kappa_-$ that correspond to L_1 halo family (right), from $1:2 \kappa_-$ that correspond to L_2 and L_3 vertical Lyapunov branch (middle), and from $1:3 \kappa_-$ that form bridge families to $1:1 A1$ and to $1:1 \kappa_+$ (left).

and think families indicate doubly and simple symmetric solutions, correspondingly. Edges at branch points associated to planar orbits, we draw in black, vertically and shortly before and after the bifurcations. Edges of vertical bifurcations we draw in red or blue: if the bifurcated branch begins with the same index as the underlying comet orbits before the bifurcation, then the bifurcated branch is a *red branch*, otherwise a *blue branch*. Symmetric branches that are obtained by σ -symmetry (reflection at the ecliptic) have same color and are dashed. Families labeled with overlined index indicate bad orbits. By “b-d” we denote birth-death bifurcation, whose local Floer homology and its Euler characteristic are zero.

(1) *Bifurcations from 1:1 and 1:2 retrograde κ_- orbit.* The out-of-plane bifurcated branches from 1:1 and 1:2 retrograde κ_- orbit are well-known: The one that bifurcates from 1:1 κ_- corresponds to the

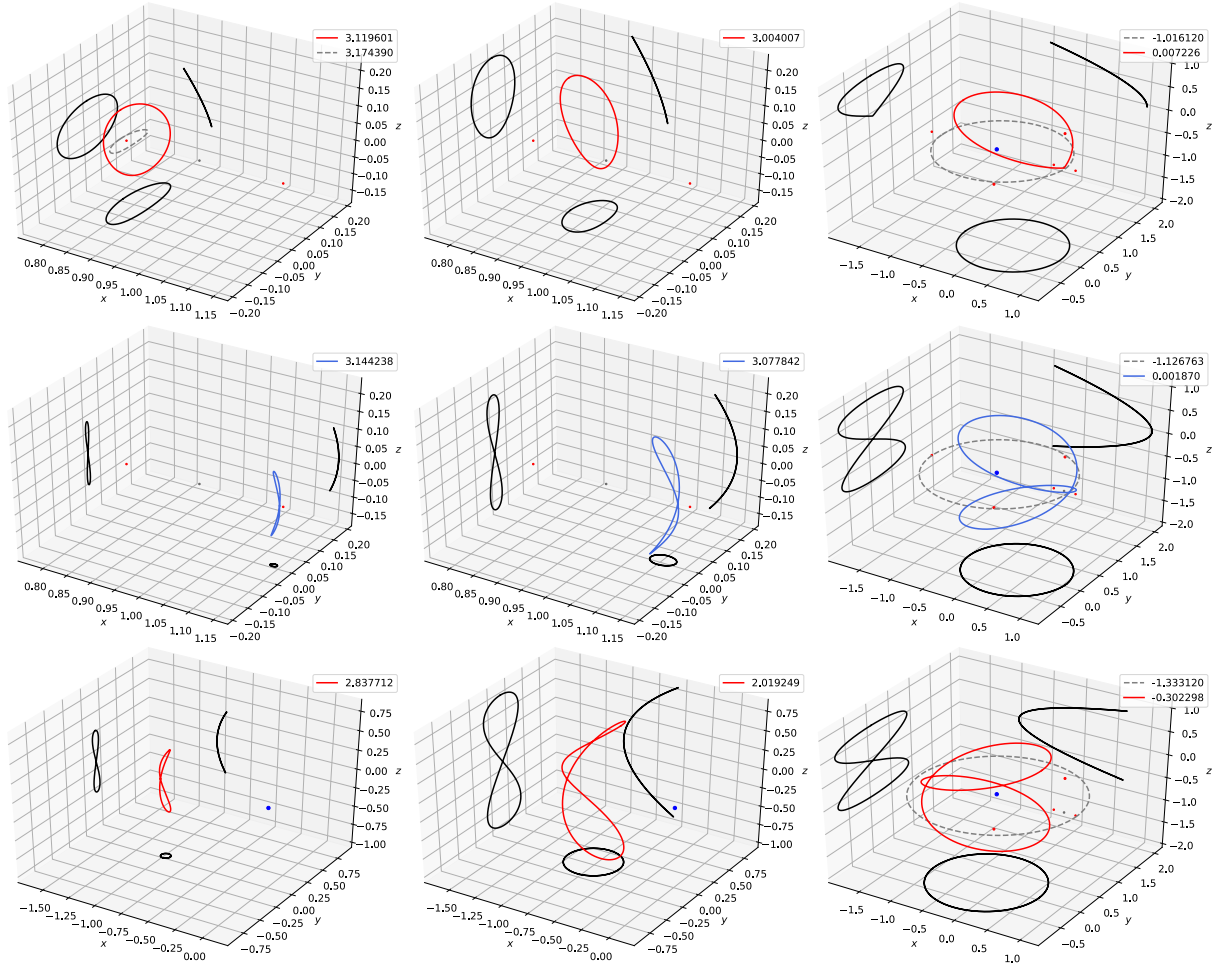


Figure 7: Top shows some orbits, ordered from right to left, of L_1 halo branch generated from 1:1 retrograde comet κ_- orbit (grey dashed right) and terminating at L_1 planar Lyapunov orbit (grey dashed left). Middle, from right to left, shows some orbits of L_2 vertical Lyapunov branch generated from 1:2 κ_- (grey dashed right) and terminating at L_2 . Bottom, from right to left, shows some orbits of L_3 vertical Lyapunov orbits generated from 1:2 κ_- (grey dashed right) and terminating at L_3 .

family of L_1 halo orbits which are usually computed from L_1 planar Lyapunov orbits, and the ones that bifurcate from the two critical 1:2 κ_- orbits correspond to the branch of L_2 and L_3 vertical Lyapunov orbits which are of figure-eight shape and usually generated around corresponding libration points. The bifurcation graphs that illustrate these bifurcation results are shown in Figure 6, some orbits for certain Jacobi constant values are plotted in Figure 7, and data base are collected in Table A2. Let us discuss that bifurcations from comet orbits are in accordance with the Euler characteristic. In the case of 1:1 κ_- orbit, before the branch point there are only the comet orbits with index 2, and after the branch point the comet orbits have index 3 and each of the two L_1 halo branches has index 2. Therefore, the Euler characteristic before and after the bifurcation point is correspondingly

$$(-1)^2 = 1, \quad 2 \cdot (-1)^2 + (-1)^3 = 1.$$

Within the period-doubling branching off from the two 1:2 κ_- orbits we obtain our first example where bad orbits occur. These bad orbits appear as period-doubling of the retrograde comet orbits that are vertically negative hyperbolic, and planar elliptic, in the Jacobi constant range $(-1.333119, -1.126762)$, see Figure 4. They have index $\bar{3}$ as denoted in the bifurcation diagram in the middle of Figure 6. So, at the first branch point of the 1:2 κ_- orbit, the period-doubling comet orbits before the bifurcation have index 2, and after the bifurcation they have index $\bar{3}$, while the bifurcated L_3 vertical Lyapunov orbits

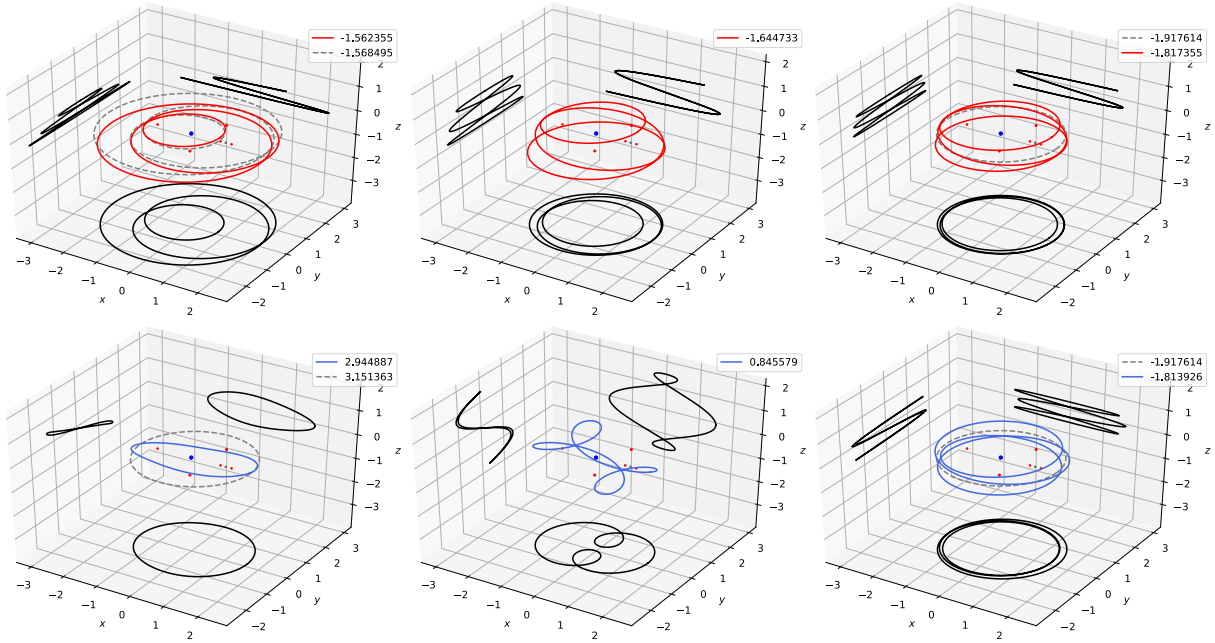


Figure 8: Top and bottom, from right to left, shows some orbits of red and blue branch that bifurcate from 1:3 κ_- (grey dashed right). Red branch forms a bridge to 1:1 A1 (grey dashed left), and blue branch forms a bridge to 1:1 κ_+ (grey dashed left).

have index 2. Therefore, the Euler characteristic before and after bifurcation is $(-1)^2 = 1$ in each case. Furthermore, at the second branch point of the 1:2 κ_- orbit, before the bifurcation there are only the bad comet orbits with index $\bar{3}$, and after the bifurcation the period-doubling comet orbits have index 4, while the bifurcated L_2 vertical Lyapunov orbits have index 3. Hence, the Euler characteristic before and after the branch point equals zero.

(2) *Bifurcation from 1:3 retrograde κ_- orbit.* At the Jacobi constant value $C \approx -1.917613$ the Conley–Zehnder index of the 3-covering of the 1:3 κ_- orbit with period $T \approx 12.619274$ jumps from 2 to 4. The members of the red branch (they start with index 2) are simple symmetric w.r.t. XOZ -symmetry, and the orbits of the blue branch (they start with index 3) are simple symmetric w.r.t. OX -symmetry. Each of the two branches has a symmetric branch by using the σ -symmetry (reflection at the ecliptic), corresponding to dashed families in the bifurcation diagram in Figure 6. Some orbits are plotted in Figure 8, and data are provided in Table A3. The red branch grows, as z increases to the value $z \approx 0.535093$ at $C \approx -1.644732$, and then the initial parameter z decreases. Then, after a birth-death bifurcation at $C \approx -1.552974$, it terminates planar at $C \approx -1.568494$ on a vertical-critical orbit that belongs to the family of retrograde periodic solutions around the Earth denoted by A1 in Broucke’s notation [10]. All periodic orbits of the red family with Conley–Zehnder index 2 are stable. The blue branch grows until to $z \approx 0.808557$ at $C \approx 0.845579$, and then it goes down to plane on the second critical 1:1 direct κ_+ orbit at $C \approx 3.151363$. This is our first example of a bridge family between retrograde and direct comet orbits that consists of spatial periodic solutions. Along the continuation of the blue branch, some loops appear and disappear on the orbits, as can be seen in Figure 8. Blue orbits are entirely unstable, with being elliptic and positive hyperbolic (with index 3) and purely positive hyperbolic (with index 4).

(3) *Bifurcation from 1: k retrograde κ_- orbit ($k = 4, 5, 6$).* The vertical self-resonant bifurcations of the 1: k retrograde κ_- orbits all produce the same results, for $k = 4, 5, 6$. For each k , all the vertically bifurcated branches terminate planar at the \tilde{k} -covering of the 1: \tilde{k} direct κ_+ orbits, with $\tilde{k} = k - 2$. Therefore, for each k , we obtain bridge families between the 1: k retrograde κ_- and the 1: \tilde{k} direct κ_+ orbits. The bifurcation diagrams are shown in Figure 9, with orbit plots in Figure 10, Figure 11 and Figure 12. The geometric shape of the orbits of the bifurcated branches is similar: various loops appear and disappear on the orbits. Moreover, for each k , the Conley–Zehnder index of the k -covering of the 1: k retrograde

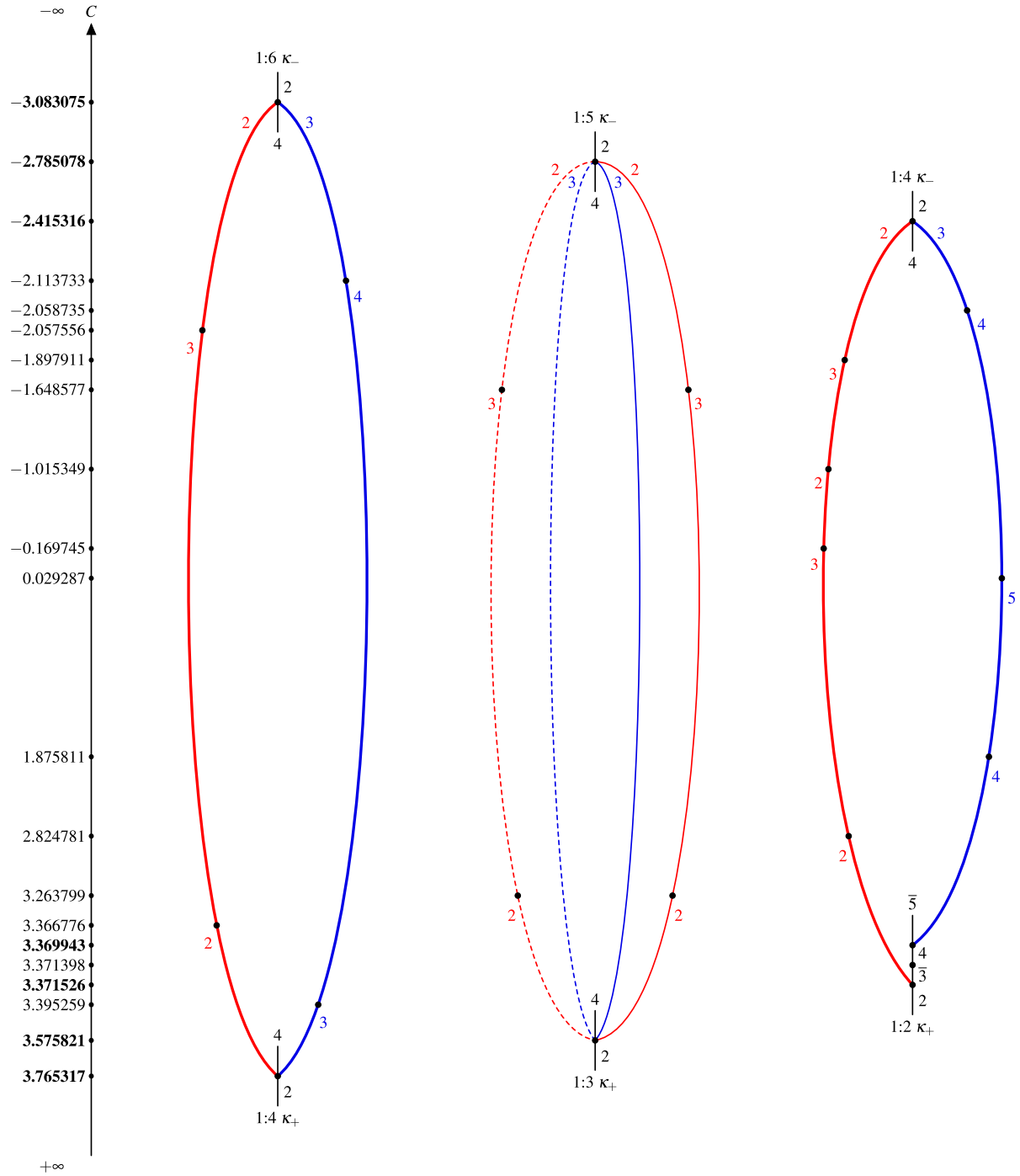


Figure 9: Bifurcation graph related to the bridge families between the $1:k$ retrograde κ_- and the $1:(k-2)$ direct κ_+ orbits, with $k = 4, 5, 6$.

κ_- orbits jumps from 2 to 4. That is because the linearized flow along the comet orbits rotates rather slowly, and the vertical direction is slightly faster than the planar one. For the $1:\tilde{k}$ direct κ_+ orbits, the index of the \tilde{k} -covering also jumps from 2 to 4, for $\tilde{k} = 4, 3$. If $\tilde{k} = 2$, then due to various negative hyperbolic phases of the planar and vertical stability indices (see Figure 5), the Conley–Zehnder index of the period-doubling of $1:2$ direct κ_+ orbits first goes from 2 to $\bar{3}$ (bad orbits), then from $\bar{3}$ to 4, and then from 4 to $\bar{5}$ (bad again). This index behavior of the retrograde and direct comet orbits is vastly contrasting to what we are aware of and have studied about the retrograde and direct periodic orbits generated by very small Keplerian solutions near one of the primaries [3–6, 37].

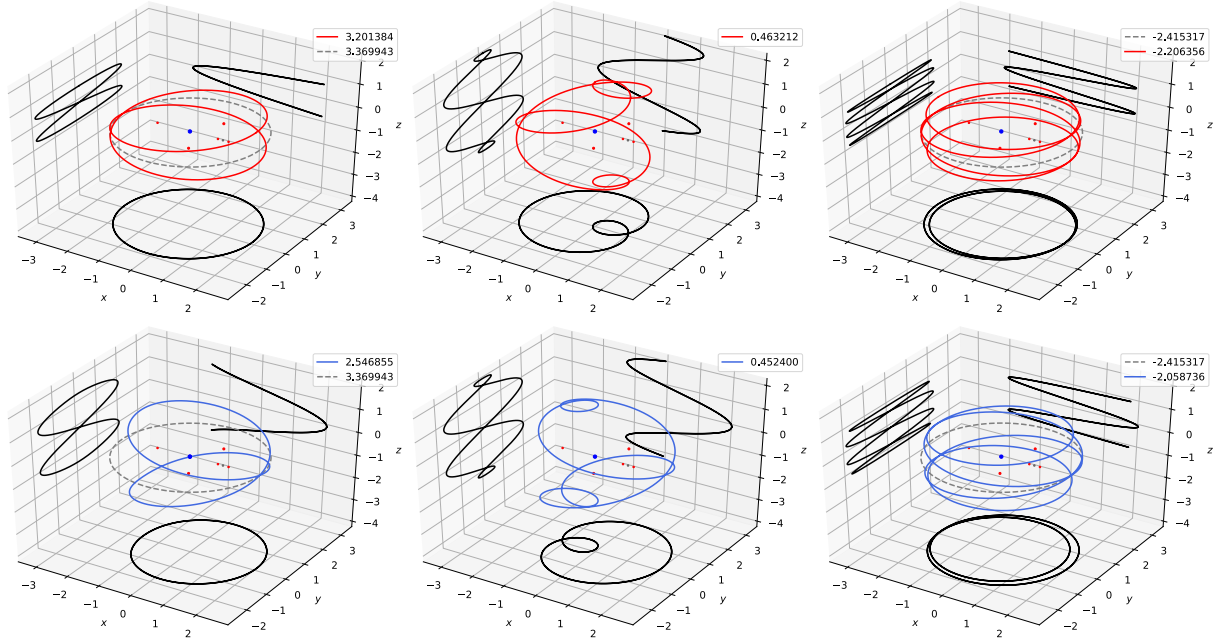


Figure 10: Orbits of red and blue branch forming bridge, from right to left, between 1:4 retrograde κ_- (grey dashed right) and 1:2 direct κ_+ orbits (grey dashed left).

(3a) *Bridge between 1:4 retrograde κ_- and 1:2 direct κ_+ orbits.* Orbits of the red and blue branches generated from 4-covering of the 1:4 retrograde κ_- orbit with period $T \approx 18.870232$ at $C \approx -2.415316$ are doubly symmetric w.r.t. XOZ - OZ and OX - XOZ -symmetry, correspondingly. Some orbits are plotted in Figure 10 and data base are listed in Table A4. By inspection the orbit plots in Figure 10, it seems that there is a YOZ -symmetry with respect to the origin, which relates the red and blue families. Along the continuation of the red branch, the Conley–Zehnder index moves several times between 2 and 3 (see Figure 9), and all those with index 2 are stable. The initial parameter z reaches a maximum value $z \approx 2.077839$ at $C \approx 0.463212$, then it decreases and terminates planar at the first period-doubling branch point of 1:2 direct κ_+ orbit at $C \approx 3.371526$. Concerning the blue branch, the initial parameter \dot{z} takes a peak at $\dot{z} \approx 0.693535$ at $C \approx 0.452400$, and then it goes down to plane on the second period-doubling bifurcation point of 1:2 direct κ_+ orbit at $C \approx 3.369943$. Members of the blue branch have Conley–Zehnder indices 3, 4, or 5 (see Figure 9), being entirely unstable. The periodic orbits with index 3 and 5 are of elliptic and positive hyperbolic type, while the orbits with index 4 are purely positive hyperbolic.

(3b) *Bridge between 1:5 retrograde κ_- and 1:3 direct κ_+ orbits.* From the 5-covering of the 1:5 retrograde κ_- orbit with period $T \approx 25.572403$ at $C \approx -2.785078$, orbits of the red and blue branches are simple symmetric w.r.t. OX - and XOZ -symmetry, respectively. By applying the σ -symmetry (reflection at the ecliptic), each of the two branches has a symmetric branch (dashed in Figure 9). Plots of some orbits are provided in Figure 11 and data base can be found in Table A5. Both branches terminate at the 3-covering of the 1:3 direct κ_+ orbit at $C \approx 3.575821$. The blue branch consists entirely of orbits that are of elliptic and positive hyperbolic type, with constant Conley–Zehnder index 3. The maximum value of the initial parameter z is $z \approx 1.735593$ at $C \approx -0.817202$. Along the continuation of the red branch, orbits first start with index 2, then the index jumps to 3, and then it jumps back to 2. The orbits with index 2 are all stable, while those with index 3 are of elliptic and positive hyperbolic type. The vertical initial parameter \dot{z} reaches a maximum value $\dot{z} \approx 0.812872$ at $C \approx -0.192251$.

(3c) *Bridge between 1:6 retrograde κ_- and 1:4 direct κ_+ orbits.* The 6-covering of the vertical-critical 1:6 retrograde κ_- orbit at $C \approx -3.083075$ has a period of $T \approx 31.424192$. At this branch point, the bifurcated orbits of the red and blue branch are doubly symmetric w.r.t. OX - XOZ -symmetry. Some orbits are plotted in Figure 12 and data are provided in Table A6. Both families terminate at a plane on the 1:4 direct κ_+ orbit at $C \approx 3.765317$. Similar to the case (3a), in view of the orbit's geometry

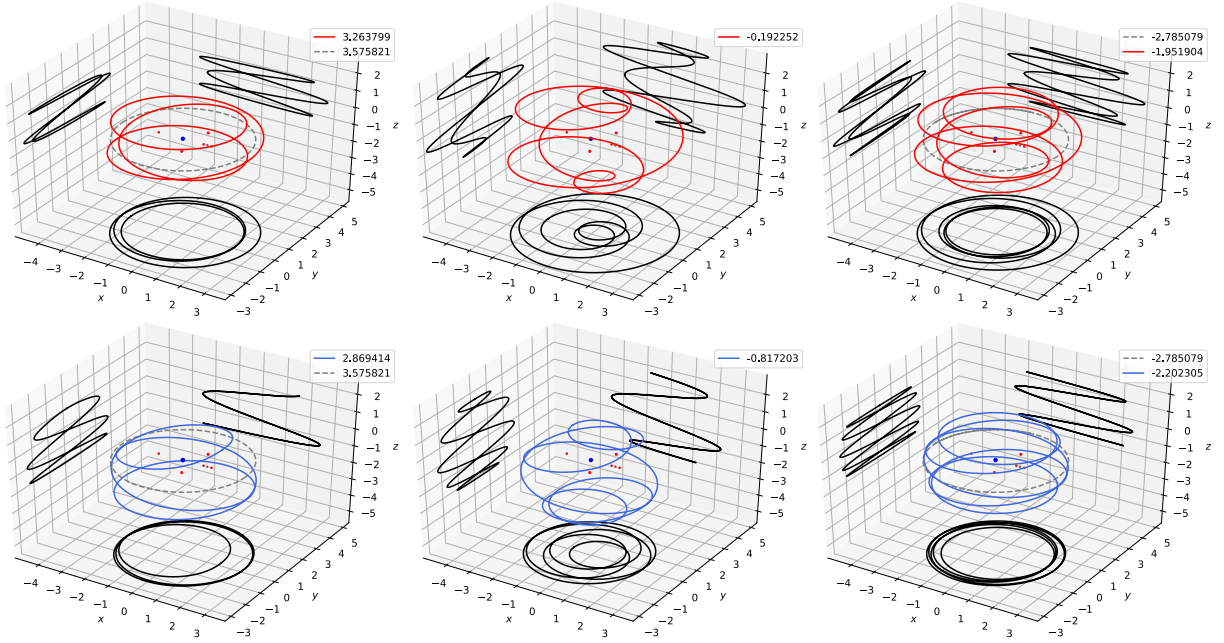


Figure 11: Orbits of red and blue branch forming bridge, from right to left, between 1:5 retrograde κ_- (grey dashed right) and 1:3 direct κ_+ orbits (grey dashed left).

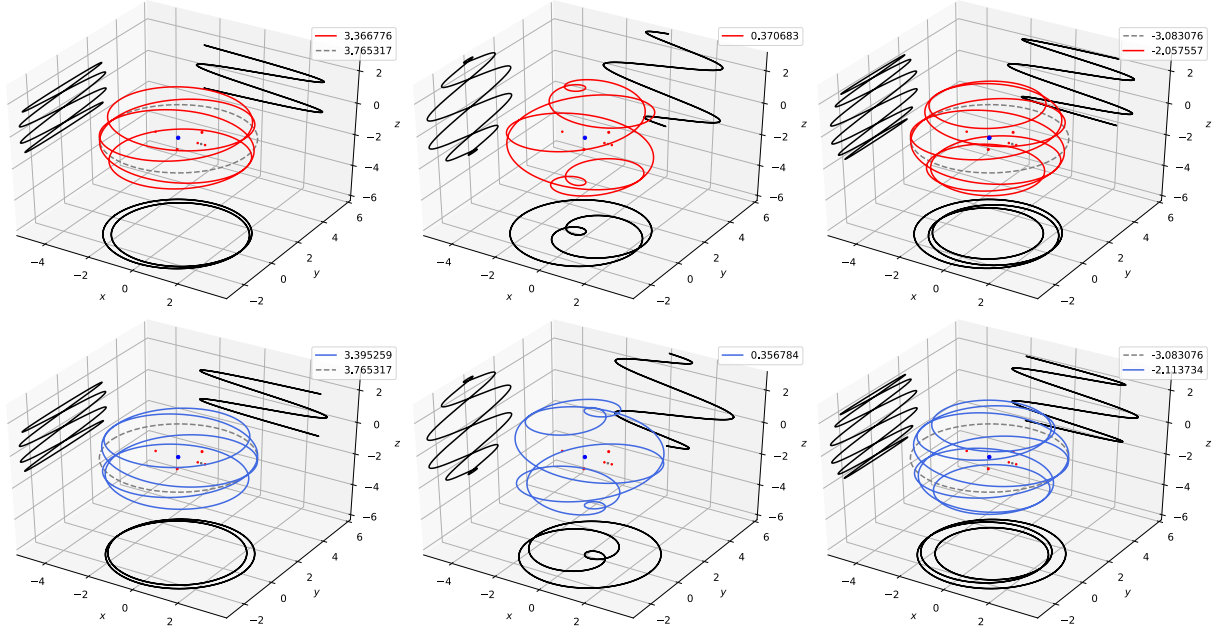


Figure 12: Orbits of red and blue branch forming bridge, from right to left, between 1:6 retrograde κ_- (grey dashed right) and 1:4 direct κ_+ orbits (grey dashed left).

in Figure 12, it seems that there is a YOZ -symmetry with respect to the origin, which connects both branches. As before, the red branch consists of orbits that start with Conley–Zehnder index 2, then jumps to 3, and then jumps back to 2 before reaching the 1:4 direct κ_+ orbit. All the orbits with index 2 are stable, while those with index 3 are of elliptic and positive hyperbolic type. The out-of-plane initial parameter \dot{z} reaches a maximum value $\dot{z} \approx 0.585070$ at $C \approx 0.370683$. Members of the blue branch start with index 3, then jumps to 4, and then jumps back to 3. All orbits are unstable, being elliptic and positive hyperbolic with index 3, and purely positive hyperbolic with index 4. The maximum value of the initial parameter \dot{z} is $\dot{z} \approx 0.584669$ at $C \approx 0.356784$.

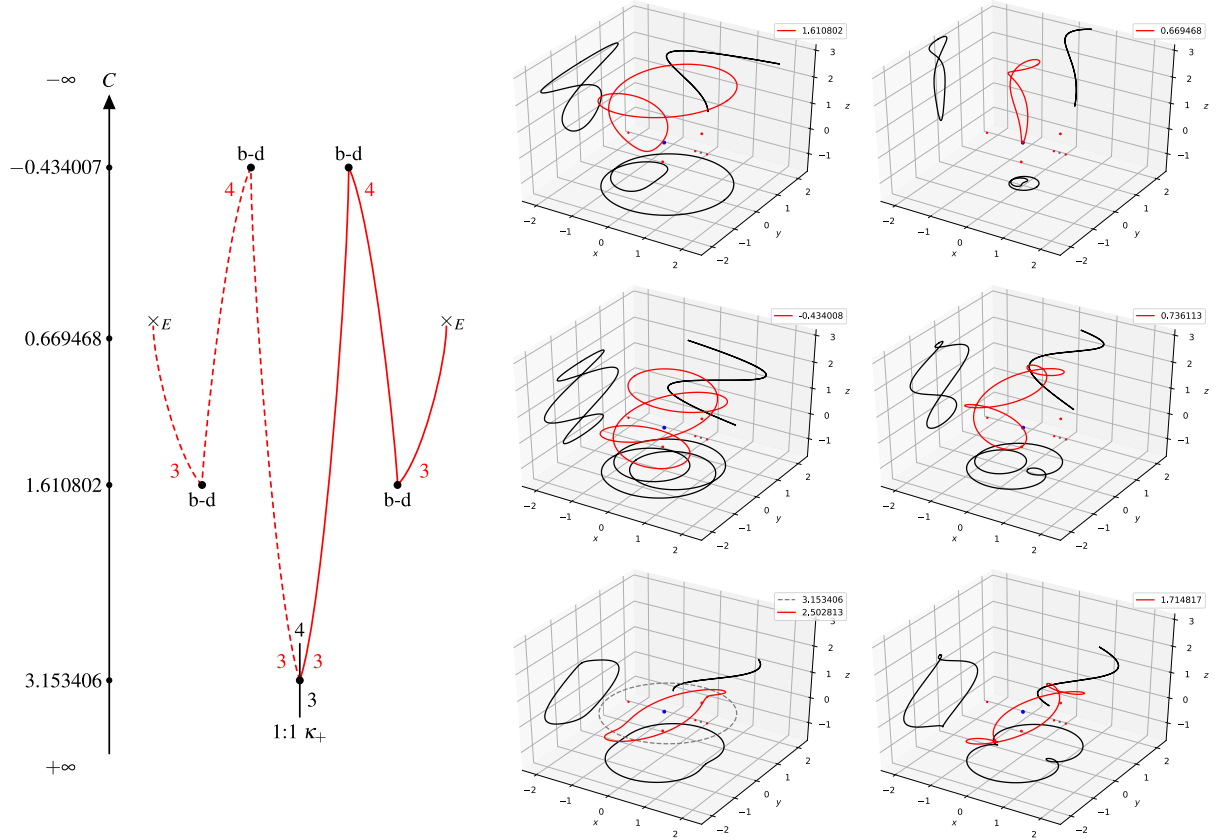


Figure 13: Left: Bifurcation diagram associated to vertically bifurcated branch from 1:1 κ_+ that is continued up to approaching collision with the Earth indicated by \times_E . Right: Orbit plots that are ordered row-wise, from bottom left (grey dashed corresponds to 1:1 κ_+) to top right.

(4) *Bifurcation from 1:1 direct κ_+ orbit.* From the second vertical-critical 1:1 direct κ_+ orbit at $C \approx 3.153406$ we generate a branch whose orbits are simple symmetric w.r.t. XOZ -symmetry. Since one can increase or decrease with the out-of-plane initial parameter z , by using the σ -symmetry (reflection at the ecliptic) one obtains a symmetric branch. The resulting bifurcation graph together with some orbit plots are shown in Figure 13, and data base are provided in Table A7. At the 1:1 κ_+ orbit the Conley–Zehnder index jumps from 3 to 4, and the members of the bifurcated branch in decreasing direction of the Jacobi constant start with index 3 being of elliptic and positive hyperbolic type. After a long continuation the branch undergoes a birth-death bifurcation at $C \approx -0.434007$, from which the orbits are purely positive hyperbolic with index 4. Then, the family can be continued until $C \approx 1.610802$ meeting a second birth-death bifurcation point, from which the orbits are of elliptic and positive hyperbolic type again. As can be appreciated in Figure 13, along the continuation there appears and disappears several loops on the orbits, that approach collision with the Earth at $C \approx 0.669468$ where we stopped with the continuation. The initial parameter z of the last computed orbit has a value $z \approx 3.099295$. The orbit's geometry in the near-collision phase is of special shape: most of the period the orbits are far from the Earth with a large excursion of hook-shaped form in the vertical direction, so that the near-collision moment is very brief, as shown in the right top in Figure 13. This kind of orbit is so far only known for small mass values, as bifurcation from vertical collision orbits in the rotating Kepler problem [7, 8].

6 Conclusion

We studied the comet-type periodic orbits and their out-of-plane self-resonant bifurcations in the CR3BP dynamics. Comet orbits are those that are generated from very large retrograde and direct Keplerian motions around the common center of mass of the primaries. The comet orbits that are generated from

		symmetries	Conley–Zehnder index
1:1 κ_-	$\hat{\equiv}$	XOZ	2,3,4,3
1:2 κ_-	$\hat{\equiv}$	$XOZ-OX$	3,4,5
1:2 κ_-	$\hat{\equiv}$	$XOZ-OX$	2,3,4,5
1:3 κ_-	\leftrightarrow	XOZ	2,3
1:3 κ_-	\leftrightarrow	OX	3,4
1:4 κ_-	\leftrightarrow	$XOZ-OX$	2,3,2,3,2
1:4 κ_-	\leftrightarrow	$OX-XOZ$	3,4,5,4
1:5 κ_-	\leftrightarrow	OX	2,3,2
1:5 κ_-	\leftrightarrow	XOZ	3
1:6 κ_-	\leftrightarrow	$OX-XOZ$	2,3,2
1:6 κ_-	\leftrightarrow	$OX-XOZ$	3,4,3
1:1 κ_+	\leftarrow	XOZ	3,4,3

Figure 14: Bifurcation results. “ $\hat{\equiv}$ ” indicates correspondence of the bifurcated branch from left critical orbit with the right branch. Double arrows indicate bridge families between left and right critical orbits with corresponding $1:k$ self-resonance. At bottom, left arrow indicates non-closed branch that approach collision with the Earth denoted by \times_E . Orbits with Conley–Zehnder index 2 provide stable solutions.

the retrograde ones are denoted by κ_- and those that are generated from the direct ones are denoted by κ_+ . We first discussed an analytical proof of their existence in Theorem 4.1, based on the classical Poincaré continuation method. Within this analytical approach, we also determine the Conley–Zehnder index, defined as a Maslov index using a crossing form. Since the Conley–Zehnder index leads to a grading on a topological bifurcation invariant, the local Floer homology and its Euler characteristic, the computation of the Conley–Zehnder index provides a systematic bifurcation analysis. Within the Earth–Moon CR3BP framework, we explored numerically the two families κ_{\pm} and their vertical self-resonant bifurcations. We computed the planar and vertical stability indices of comet orbits κ_{\pm} , identified vertical self-resonant orbits up to multiplicity six, analyzed the vertically bifurcated branches and bridge families, and discussed their orbital characteristics. Detailed descriptions, along with bifurcation diagrams and orbit plots, are provided in Section 5. Our main bifurcation results are summarized in Figure 14. It is noteworthy that the bifurcation structure of the bridges among retrograde and direct comet orbits is similar to that associated with retrograde and direct solutions generated by small Keplerian motions near one of the primaries studied in [3–6, 37], namely that two more coverings of the retrograde are always necessary to form a spatial bridge to the direct orbit. In contrast to the small direct and retrograde orbits, where the Conley–Zehnder index of the multiple-coverings becomes very high, the multiple-coverings of the retrograde and direct comet orbits always have an index jump from 2 to 4, due to the very slow rotation of the linearized flow along the comet orbits.

Appendix Tables of data

The database contains initial data, Floquet multipliers with corresponding Krein signatures and Conley–Zehnder indices of selected orbits associated to the families we have studied. For a pair of hyperbolic Floquet multipliers we denote by λ the one with $|\lambda| > 1$. For a pair of elliptic Floquet multipliers we denote by θ the rotation angle modulo 2π characterized by Krein signature. Horizontal dashed lines indicate birth-death bifurcations.

Table A1: Data for κ_- (first block) and κ_+ (second block).

C	$x(0)$	$\dot{y}(0)$	$T/2$	Floquet multipliers & Krein sign	$\mu_{CZ} / \mu_{CZ}^p / \mu_{CZ}^s$
-3.73079020	3.96375030	-4.46622787	2.788167	(+) $\theta_p \approx 0.706$, (+) $\theta_s \approx 0.707$	2 / 1 / 1
-3.08307598	2.92838023	-3.51324570	2.618682	(+) $\theta_p \approx 1.044$, (+) $\theta_s \approx 2\pi/6$	2 / 1 / 1
-2.78507825	2.52551891	-3.15557876	2.514480	(+) $\theta_p \approx 1.251$, (+) $\theta_s \approx 2\pi/5$	2 / 1 / 1
-2.41531689	2.08857210	-2.78208822	2.358779	(+) $\theta_p \approx 1.560$, (+) $\theta_s \approx 2\pi/4$	2 / 1 / 1
-1.91761341	1.60566275	-2.39923349	2.103212	(+) $\theta_p \approx 2.059$, (+) $\theta_s \approx 2\pi/3$	2 / 1 / 1
-1.33311990	1.17816938	-2.12337566	1.742922	(+) $\theta_p \approx 2.650$, $\lambda_s \approx -1.000$	2 / 1 / 1
-1.19019267	1.09454322	-2.09792012	1.634914	(+) $\theta_p \approx 2.741$, $\lambda_s \approx -1.397$	2 / 1 / 1
-1.12676203	1.06081793	-2.10393894	1.574541	(+) $\theta_p \approx 2.934$, $\lambda_s \approx -1.000$	2 / 1 / 1
-1.06179859	1.03118167	-2.14002812	1.490894	$\lambda_p \approx -2.251$, (-) $\theta_s \approx 2\pi/3$	2 / 1 / 1
-1.04060107	1.02363545	-2.16219513	1.456837	$\lambda_p \approx -3.079$, (-) $\theta_s \approx 2\pi/4$	2 / 1 / 1
-1.01611986	1.01670394	-2.19373120	1.414661	$\lambda_p \approx -4.550$, $\lambda_s \approx 1.000$	2 \rightarrow 3 / 1 / 1 \rightarrow 2
-0.48769543	-0.27646347	2.83871407	0.796606	$\lambda_p \approx -57.70$, $\lambda_s \approx 300.5$	3 / 1 / 2
-0.41303508	-0.17803693	3.51792654	0.671272	(+) $\theta_p \approx 2.760$, $\lambda_s \approx 533.5$	3 / 1 / 2
-0.41292572	-0.17508887	3.54826837	0.667245	(+) $\theta_p \approx 0.019$, $\lambda_s \approx 544.3$	3 / 1 / 2
-0.41292568	-0.17508886	3.54826847	0.667244	$\lambda_p \approx 1.004$, $\lambda_s \approx 544.3$	2 / 0 / 2
-0.95924764	-0.06168512	6.39335159	0.477327	$\lambda_p \approx 848.9$, $\lambda_s \approx 1926$	2 / 0 / 2
-1.68063393	-0.04012751	8.50504725	0.417761	$\lambda_p \approx 2135$, $\lambda_s \approx 3554$	2 / 0 / 2
-2.51369826	-0.02999931	10.64223834	0.378057	$\lambda_p \approx 4033$, $\lambda_s \approx 5797$	2 / 0 / 2
3.94727405	3.32100001	-2.77216975	3.763832	(+) $\theta_p \approx 1.243$, (+) $\theta_s \approx 1.245$	2 / 1 / 1
3.76531791	2.92763105	-2.34313685	3.925946	(+) $\theta_p \approx 1.566$, (+) $\theta_s \approx 2\pi/4$	2 / 1 / 1
3.57582149	2.52462303	-1.89539901	4.186777	(+) $\theta_p \approx 2.086$, (+) $\theta_s \approx 2\pi/3$	2 / 1 / 1
3.37152656	2.09036920	-1.39994341	4.704335	(+) $\theta_p \approx 3.134$, $\lambda_s \approx -1.000$	2 / 1 / 1
3.37139816	2.09009402	-1.39962427	4.704806	$\lambda_p \approx -1.000$, $\lambda_s \approx -1.003$	2 / 1 / 1
3.36994316	2.08697533	-1.39600678	4.710158	$\lambda_p \approx -1.021$, $\lambda_s \approx -1.000$	2 / 1 / 1
3.36445490	2.07520682	-1.38234813	4.730661	$\lambda_p \approx -1.000$, (-) $\theta_s \approx 3.188$	2 / 1 / 1
3.26371835	1.85842481	-1.12877794	5.226019	(-) $\theta_p \approx 4.150$, (-) $\theta_s \approx 2\pi/3$	2 / 1 / 1
3.22782403	1.78256000	-1.03977090	5.484844	(-) $\theta_p \approx 4.668$, (-) $\theta_s \approx 2\pi/4$	2 / 1 / 1
3.15340606	1.69254257	-0.95118846	6.254196	$\lambda_p \approx 1.473$, $\lambda_s \approx 1.000$	3 \rightarrow 4 / 2 / 1 \rightarrow 2
3.15194964	1.69613732	-0.95696577	6.268160	$\lambda_p \approx 1.498$, $\lambda_s \approx 1.017$	4 / 2 / 2
3.15136315	1.69775817	-0.95952922	6.273520	$\lambda_p \approx 1.508$, $\lambda_s \approx 1.000$	4 \rightarrow 5 / 2 / 2 \rightarrow 3
3.15055237	1.70016298	-0.96329648	6.280659	$\lambda_p \approx 1.521$, (+) $\theta_s \approx 0.027$	5 / 2 / 3
2.98165907	2.17197153	-1.63122614	6.324042	$\lambda_p \approx 3.678$, (+) $\theta_s \approx 0.106$	5 / 2 / 3
1.49947321	3.07313502	-2.93201321	6.274403	$\lambda_p \approx 2.319$, (+) $\theta_s \approx 0.016$	5 / 2 / 3

Table A2: Data for orbit families branching off from 1:1 κ_- corresponding to L_1 halo (first block), from 1:2 κ_- corresponding to L_2 and L_3 vertical Lyapunov (second and third block, respectively).

C	$x(0)$	$z(0)$	$\dot{y}(0)$	$T/2$	Floquet multipliers & Krein sign	μ_{CZ}
-1.01611986	-0.84576821	0	2.02848068	1.414661	$\lambda_p \approx -4.550, \lambda_s \approx 1.000$	$2 \rightarrow 3$
-1.01121740	-0.84802264	0.04500000	2.02578862	1.417869	$\lambda \approx -4.980, (-) \theta \approx 5.264$	2
-0.98614733	-0.86050440	0.11500000	2.01183966	1.435595	$\lambda_1 \approx -7.801, \lambda_2 \approx -1.194$	2
1.00758977	-0.00588985	0.99501230	0.99764024	1.556055	$513.3 \pm 376.2i, 0.001 \pm 0.001i$	2
2.94065356	0.92852311	0.29459187	0.08181840	1.083121	$(-) \theta_1 \approx 4.661, (+) \theta_2 \approx 1.626$	2
2.94342187	0.92915408	0.29140652	0.08174723	1.075469	$(-) \theta \approx 5.504, \lambda \approx -1.000$	2
2.94699116	0.92992363	0.28728227	0.08174985	1.065406	$\lambda_1 \approx 1.000, \lambda_2 \approx -2.623$	$2 \rightarrow 3$
2.97165710	0.93338449	0.25816317	0.08596446	0.990270	$\lambda_1 \approx 2.373, \lambda_2 \approx -5.415$	3
3.00400727	0.91276840	0.20718952	0.15444698	0.915881	$\lambda_1 \approx 1.001, \lambda_2 \approx -4.433$	3
3.00400727	0.91276832	0.20718947	0.15444717	0.915881	$(+) \theta \approx 0.001, \lambda \approx -4.433$	4
2.99862220	0.88116552	0.19373322	0.22165687	1.056634	$(+) \theta \approx 0.924, \lambda \approx -1.000$	4
2.99783519	0.87193582	0.19019461	0.23730262	1.115036	$(+) \theta_1 \approx 0.002, (+) \theta_2 \approx 1.957$	4
2.99783519	0.87193578	0.19019460	0.23730267	1.115037	$\lambda \approx 1.002, (+) \theta \approx 1.957$	3
3.00741394	0.85032515	0.17588652	0.26274287	1.274440	$\lambda \approx 21.53, (+) \theta \approx 2.571$	3
3.11960141	0.82631121	0.08588652	0.20029568	1.389850	$\lambda \approx 838.4, (-) \theta \approx 5.342$	3
3.17439048	0.82336756	0	0.12634016	1.371476	$\lambda_p \approx 2361, \lambda_s \approx 1.000$	$3 \rightarrow 4$
C	$x(0)$	$\dot{y}(0)$	$\dot{z}(0)$	$T/4$	Floquet multipliers & Krein sign	μ_{CZ}
-1.12676203	1.06081793	-2.10393894	0	1.574541	$(-) \theta_p \approx 5.868, \lambda_s \approx 1.000$	$3 \rightarrow 4$
-1.12353182	1.06075604	-2.10251315	0.05499999	1.574389	$(-) \theta \approx 5.942, \lambda \approx 1.406$	3
-1.11699017	1.06077019	-2.09942385	0.09698150	1.574377	$\lambda_1 \approx 1.000, \lambda_2 \approx 1.819$	$3 \rightarrow 4$
0.00187071	1.06404466	-1.57176890	0.90260590	1.571456	$\lambda_1 \approx 12.87, \lambda_2 \approx 91.99$	4
1.00449875	1.06930182	-1.10176890	1.02485766	1.565515	$\lambda_1 \approx 17.71, \lambda_2 \approx 245.3$	4
2.96706753	1.11194442	-0.18118227	0.43588315	1.105549	$\lambda_1 \approx 1.000, \lambda_2 \approx 335.3$	$4 \rightarrow 5$
3.07784218	1.13162660	-0.06764894	0.30751995	0.935413	$(+) \theta \approx 0.613, \lambda \approx 823.9$	5
3.14423876	1.14839882	-0.01733906	0.16751995	0.890856	$(+) \theta \approx 0.401, \lambda \approx 1550$	5
3.16764037	1.15450857	-0.00269836	0.06751995	0.881078	$(+) \theta \approx 0.294, \lambda \approx 1908$	5
C	$x(0)$	$z(0)$	$\dot{y}(0)$	$T/4$	Floquet multipliers & Krein sign	μ_{CZ}
-1.33311990	1.17816938	0	-2.12337566	1.742922	$(-) \theta_p \approx 5.300, \lambda_s \approx 1.000$	$2 \rightarrow 3$
-1.29018584	1.15485565	0.10500000	-2.10552729	1.729236	$(-) \theta_1 \approx 5.494, (-) \theta_2 \approx 5.725$	2
-1.08659142	1.04597982	0.24798430	-2.02336264	1.658151	$\lambda \approx 1.000, (-) \theta \approx 5.694$	$2 \rightarrow 3$
-0.88712597	0.94352218	0.38500000	-1.93846655	1.601378	$\lambda \approx 1.121, (-) \theta \approx 5.970$	3
-0.64402169	0.82132984	0.56898610	-1.82135383	1.577771	$\lambda_1 \approx 1.577, \lambda_2 \approx 1.000$	$3 \rightarrow 4$
-0.30229740	0.64993844	0.75193521	-1.65111433	1.569487	$\lambda_1 \approx 1.399, \lambda_2 \approx 1.032$	4
0.03075099	0.48299074	0.86792609	-1.48457007	1.566650	$\lambda_1 \approx 1.605, \lambda_2 \approx 1.000$	$4 \rightarrow 5$
1.00587257	-0.00506155	0.99597899	-0.99752434	1.563844	$\lambda \approx 2.106, (+) \theta \approx 0.029$	5
2.01924928	-0.51088663	0.86011032	-0.49289975	1.562901	$\lambda \approx 2.582, (+) \theta \approx 0.032$	5
2.83771288	-0.91834774	0.40635136	-0.08648728	1.562522	$\lambda \approx 2.959, (+) \theta \approx 0.032$	5
3.00893966	-1.00346817	0.05635136	-0.00159211	1.562464	$\lambda \approx 3.038, (+) \theta \approx 0.031$	5

Table A3: Data for two families emerging from 1:3 κ_- . Orbit in the first block terminate at 1:1 A_1 , and orbits in the second block terminate at 1:1 κ_+ .

C	$x(0)$	$z(0)$	$\dot{y}(0)$	$T/2$	Floquet multipliers & Krein sign	μ_{CZ}
-1.91761341	1.60566275	0	-2.39923349	6.309637	(-) $\theta_p \approx 6.177, \lambda_s \approx 1.000$	2 \rightarrow 4
-1.81735436	1.45213275	0.40000000	-2.29505407	6.307873	(-) $\theta_1 \approx 6.120, (-) \theta_2 \approx 6.266$	2
-1.64473200	1.19211399	0.53509332	-2.14652015	6.305408	(-) $\theta_1 \approx 5.968, (-) \theta_2 \approx 6.257$	2
-1.55297424	0.89906119	0.32676374	-2.11518547	6.322365	(-) $\theta_1 \approx 5.964, (-) \theta_2 \approx 6.280$	2
-1.55297424	0.89697817	0.32348360	-2.11596504	6.322815	(-) $\theta \approx 5.689, \lambda \approx 1.002$	3
-1.56235471	0.81383824	0.13914529	-2.16620917	6.358972	(-) $\theta \approx 5.470, \lambda \approx 1.034$	3
-1.56849475	0.79468554	0	-2.18507428	6.379428	(-) $\theta_p \approx 5.393, \lambda_s \approx 1.000$	2 \rightarrow 3
C	$x(0)$	$\dot{y}(0)$	$\dot{z}(0)$	$T/2$	Floquet multipliers & Krein sign	μ_{CZ}
-1.91761341	1.60566275	-2.39923349	0	6.309637	(-) $\theta_p \approx 6.177, \lambda_s \approx 1.000$	2 \rightarrow 4
-1.81392539	1.70156027	-2.41995114	0.20000000	6.307532	(-) $\theta \approx 6.118, \lambda \approx 1.017$	3
-1.30597461	2.02602529	-2.50444153	0.36232839	6.293265	$\lambda_1 \approx 1.000, \lambda_2 \approx 1.104$	3 \rightarrow 4
0.01978289	1.66817421	-1.85359980	0.73396077	6.283455	$\lambda_1 \approx 1.080, \lambda_2 \approx 1.772$	4
0.84557994	1.55885049	-1.49359980	0.80855708	6.281744	$\lambda_1 \approx 1.131, \lambda_2 \approx 2.425$	4
2.33904193	1.60479821	-1.07681306	0.58143972	6.276518	$\lambda_1 \approx 1.282, \lambda_2 \approx 2.617$	4
2.94488745	1.67186668	-0.98393202	0.30143972	6.274243	$\lambda_1 \approx 1.374, \lambda_2 \approx 1.807$	4
3.15136315	1.69775817	-0.95952922	0	6.273520	$\lambda_p \approx 1.508, \lambda_s \approx 1.000$	5 \rightarrow 4

Table A4: Data for two families bifurcating from 1:4 κ_- . In view of Figure 9, orbits in the first block correspond to red branch, and orbits in the second block correspond to blue branch. Both families terminate at 1:2 κ_+ .

C	$x(0)$	$z(0)$	$\dot{y}(0)$	$T/4$	Floquet multipliers & Krein sign	μ_{CZ}
-2.41531689	-2.08786757	0	2.78104740	4.717558	(-) $\theta_p \approx 6.241, \lambda_s \approx 1.000$	2 \rightarrow 4
-2.20635533	-1.93838562	0.77200000	2.63130893	4.716830	(-) $\theta_1 \approx 6.194, (-) \theta_2 \approx 6.256$	2
-1.89791187	-1.71694084	1.18249000	2.40962414	4.715987	(-) $\theta \approx 6.093, \lambda \approx 1.000$	2 \rightarrow 3
-1.55961509	-1.47338332	1.47271735	2.16593152	4.715271	(-) $\theta \approx 6.011, \lambda \approx 1.013$	3
-1.01534919	-1.08077118	1.77861858	1.77327052	4.714397	(-) $\theta \approx 5.915, \lambda \approx 1.000$	3 \rightarrow 2
-0.57577415	-0.76338453	1.93482010	1.45593152	4.713838	(-) $\theta_1 \approx 5.860, (-) \theta_2 \approx 6.273$	2
-0.16974581	-0.47016752	2.02514833	1.16279452	4.713384	(-) $\theta \approx 5.821, \lambda \approx 1.000$	2 \rightarrow 3
0.46321270	-0.01315667	2.07783917	0.70593152	4.712724	(-) $\theta \approx 5.776, \lambda \approx 1.024$	3
1.23938644	0.54697989	2.00390183	0.14593152	4.711854	(-) $\theta \approx 5.744, \lambda \approx 1.042$	3
2.82478178	1.69181204	1.21295943	-0.99968252	4.708275	(-) $\theta \approx 5.822, \lambda \approx 1.000$	3 \rightarrow 2
3.20138458	1.96566673	0.70006443	-1.27449955	4.705982	(-) $\theta_1 \approx 5.973, (-) \theta_2 \approx 6.243$	2
3.37152656	2.08697533	0	-1.39600678	4.710158	(-) $\theta_p \approx 6.269, \lambda_s \approx 1.000$	2 \rightarrow 3
C	$x(0)$	$\dot{y}(0)$	$\dot{z}(0)$	$T/4$	Floquet multipliers & Krein sign	μ_{CZ}
-2.41531689	2.08857210	-2.78208822	0	4.717558	(-) $\theta_p \approx 6.241, \lambda_s \approx 1.000$	2 \rightarrow 4
-2.23032078	2.08707669	-2.73695277	0.24199999	4.716389	(-) $\theta \approx 6.258, \lambda \approx 1.082$	3
-2.05873588	2.08606393	-2.69524723	0.33133100	4.715605	$\lambda_1 \approx 1.000, \lambda_2 \approx 1.152$	3 \rightarrow 4
-1.31916187	2.08362347	-2.51630078	0.54200000	4.713737	$\lambda_1 \approx 1.028, \lambda_2 \approx 1.408$	4
0.02928745	2.08214076	-2.19144828	0.68495225	4.712318	$\lambda_1 \approx 1.000, \lambda_2 \approx 1.762$	4 \rightarrow 5
0.45240023	2.08206794	-2.08979228	0.69353564	4.712029	(+) $\theta \approx 0.016, \lambda \approx 1.846$	5
1.87581185	2.08305464	-1.74920028	0.60725253	4.711176	$\lambda_1 \approx 1.000, \lambda_2 \approx 1.952$	5 \rightarrow 4
2.54685508	2.08433874	-1.58979228	0.48448151	4.710758	$\lambda_1 \approx 1.035, \lambda_2 \approx 1.820$	4
3.36994316	2.08697533	-1.39600678	0	4.710158	$\lambda_p \approx 1.042, \lambda_s \approx 1.000$	4 \rightarrow 5

Table A5: Data for two families branching off from 1:5 κ_- . In view of Figure 9, orbits in the first block correspond to red branch, and orbits in the second block correspond to blue branch. Both families terminate at 1:3 κ_+ .

C	$x(0)$	$\dot{y}(0)$	$\dot{z}(0)$	$T/2$	Floquet multipliers & Krein sign	μ_{CZ}
-2.78507825	-2.52523337	3.15514897	0	12.572403	(-) $\theta_p \approx 6.259, \lambda_s \approx 1.000$	2 \rightarrow 4
-1.95190358	-2.06085155	2.63081580	0.50015919	12.570616	(-) $\theta_1 \approx 6.039, (-) \theta_2 \approx 6.278$	2
-1.64857749	-1.67480758	2.28599260	0.65207487	12.570488	(-) $\theta \approx 5.994, \lambda \approx 1.000$	2 \rightarrow 3
-0.19225157	-1.84545357	2.00585092	0.81287280	12.567228	(-) $\theta \approx 6.051, \lambda \approx 1.039$	3
1.51574261	-2.00676149	1.72869916	0.72220662	12.564860	(-) $\theta \approx 5.947, \lambda \approx 1.052$	3
3.26379993	-2.24150516	1.60217526	0.29550907	12.560384	(-) $\theta \approx 6.023, \lambda \approx 1.000$	3 \rightarrow 2
3.40128178	-2.33983446	1.69790628	0.21620397	12.560137	(-) $\theta_1 \approx 6.105, (-) \theta_2 \approx 6.275$	2
3.57582149	-2.52354221	1.89368945	0	12.560333	(-) $\theta_p \approx 6.259, \lambda_s \approx 1.000$	2 \rightarrow 4
C	$x(0)$	$\dot{z}(0)$	$\dot{y}(0)$	$T/2$	Floquet multipliers & Krein sign	μ_{CZ}
-2.78507825	-2.52523337	0	3.15514897	12.572403	(-) $\theta_p \approx 6.259, \lambda_s \approx 1.000$	2 \rightarrow 4
-2.20230468	-1.96909114	1.38000000	2.62909547	12.570561	(-) $\theta \approx 6.195, \lambda \approx 1.003$	3
-0.81720281	-0.74798075	1.73559379	1.56032664	12.568861	(-) $\theta \approx 5.864, \lambda \approx 1.018$	3
1.02320791	0.34457437	1.60119923	0.56032664	12.566073	(-) $\theta \approx 5.536, \lambda \approx 1.044$	3
2.86941464	1.59425590	1.21232538	-0.81967335	12.560660	(-) $\theta \approx 5.776, \lambda \approx 1.015$	3
3.57582149	2.52462303	0	-1.89539901	12.560333	(-) $\theta_p \approx 6.259, \lambda_s \approx 1.000$	2 \rightarrow 4

Table A6: Data for two families emerging from 1:6 κ_- . In view of Figure 9, orbits in the first block correspond to red branch, and orbits in the second block correspond to blue branch. Both families terminate at 1:4 κ_+ .

C	$x(0)$	$\dot{y}(0)$	$\dot{z}(0)$	$T/4$	Floquet multipliers & Krein sign	μ_{CZ}
-3.08307598	-2.92823801	3.51302954	0	7.856048	(-) $\theta_p \approx 6.266, \lambda_s \approx 1.000$	2 \rightarrow 4
-2.82590417	-2.927444896	3.46849895	0.22200000	7.855771	(-) $\theta_1 \approx 6.270, (-) \theta_2 \approx 6.274$	2
-2.05755697	-2.92569580	3.33581052	0.41706000	7.855169	(-) $\theta \approx 6.231, \lambda \approx 1.000$	2 \rightarrow 3
0.37068395	-2.92336333	2.91854867	0.58507077	7.853980	(-) $\theta \approx 6.129, \lambda \approx 1.021$	3
3.36677655	-2.92601680	2.40917597	0.27369986	7.852301	(-) $\theta \approx 6.229, \lambda \approx 1.000$	3 \rightarrow 2
3.64903893	-2.92681861	2.36188185	0.15098786	7.852040	(-) $\theta_1 \approx 6.265, (-) \theta_2 \approx 6.269$	2
3.76531791	-2.92722927	2.34250125	0	7.851892	(-) $\theta_p \approx 6.266, \lambda_s \approx 1.000$	2 \rightarrow 4
C	$x(0)$	$\dot{y}(0)$	$\dot{z}(0)$	$T/4$	Floquet multipliers & Krein sign	μ_{CZ}
-3.08307598	2.92838023	-3.51324570	0	7.856048	(-) $\theta_p \approx 6.266, \lambda_s \approx 1.000$	2 \rightarrow 4
-2.86931536	2.92776198	-3.47626961	0.20300000	7.855811	(-) $\theta \approx 6.270, \lambda \approx 1.006$	3
-2.11373395	2.92627646	-3.34602307	0.40726000	7.855185	$\lambda_1 \approx 1.000, \lambda_2 \approx 1.049$	3 \rightarrow 4
0.35678440	2.92493645	-2.92264423	0.58466924	7.853965	$\lambda_1 \approx 1.021, \lambda_2 \approx 1.166$	4
3.39525998	2.92699047	-2.40561417	0.26413810	7.852319	$\lambda_1 \approx 1.000, \lambda_2 \approx 1.051$	4 \rightarrow 3
3.66107019	2.92741447	-2.36069292	0.14300260	7.852044	(-) $\theta \approx 6.269, \lambda \approx 1.015$	3
3.76531791	2.92763105	-2.34313685	0	7.851892	(-) $\theta_p \approx 6.266, \lambda_s \approx 1.000$	2 \rightarrow 4

Table A7: Data for branch bifurcating from 1:1 κ_+ , continued until approaching collision with the Earth.

C	$x(0)$	$z(0)$	$\dot{y}(0)$	$T/2$	Floquet multipliers & Krein sign	μ_{CZ}
3.15340606	1.69254257	0	-0.95118846	6.254196	$\lambda_p \approx 1.473, \lambda_s \approx 1.000$	3 \rightarrow 4
3.10497908	1.64057057	0.32500000	-0.89038323	6.256432	$\lambda \approx 1.418, (-) \theta \approx 5.997$	3
2.50281375	1.14121257	1.02130088	-0.32487557	6.272841	$\lambda \approx 1.284, (-) \theta \approx 5.405$	3
1.71481742	0.64318063	1.34352107	0.19512442	6.280390	$\lambda \approx 1.207, (-) \theta \approx 5.374$	3
0.61412474	-0.01215181	1.54242536	0.82470958	6.284400	$\lambda \approx 1.126, (-) \theta \approx 5.594$	3
-0.43400738	-0.81183181	1.69890129	1.69890129	6.285041	$\lambda \approx 1.193, (-) \theta \approx 6.282$	3
-0.43400072	-0.81183281	1.69891361	1.46801799	6.285041	$\bar{\lambda}_1 \approx 1.193, \bar{\lambda}_2 \approx 1.001$	4
0.73611388	0.11872418	2.40681480	0.32732843	6.274234	$\lambda_1 \approx 2.749, \lambda_2 \approx 1.044$	4
1.61080283	1.64821787	2.23796057	-1.35100956	6.264739	$\lambda_1 \approx 3.760, \lambda_2 \approx 1.001$	4
1.61080283	1.64821872	2.23796038	-1.35101056	6.264739	$\lambda \approx 3.760, (-) \theta \approx 6.283$	3
1.39262658	1.73365484	2.37502843	-1.51425179	6.258164	$\lambda \approx 3.376, (-) \theta \approx 6.243$	3
0.73257748	0.67443663	3.04798979	-1.60213845	6.211295	$\lambda \approx 2.178, (-) \theta \approx 6.122$	3
0.66946846	0.37443663	3.09929510	-1.33315327	6.159828	$\lambda \approx 1.705, (-) \theta \approx 6.025$	3

Acknowledgement. The author acknowledges support by the Deutsche Forschungsgemeinschaft (DFG, German Research Foundation), Project-ID 541062288. He also wishes to thank Urs Frauenfelder for helpful discussions. He also would like to thank Alexander Batkin and Alexander Bruno for providing English annotations from some of Bruno's preprints in Russian. Furthermore, he gratefully acknowledges Otto van Koert for valuable discussions, his warm hospitality and fostering an inspiring atmosphere during the author's stay as a visiting researcher at the Seoul National University in November 2025, where significant parts of the section on the analytical approach to comet orbits were developed.

References

- [1] Albers P., Fish J.W., Frauenfelder U., van Koert O.: *The Conley–Zehnder indices of the rotating Kepler problem.* Math. Proc. Camb. Phil. Soc. **154**(2), 243–260 (2013) <https://doi.org/10.1017/S0305004112000515>
- [2] Arnold V.I., Avez A.: *Ergodic Problems of Classical Mechanics.* New York, Benjamin (1968)
- [3] Aydin C.: *From Babylonian lunar observations to Floquet multipliers and Conley–Zehnder Indices.* J. Math. Phys. **64**(8) (2023) <https://doi.org/10.1063/5.0156959>
- [4] Aydin C.: *The Conley–Zehnder indices of the spatial Hill three-body problem.* Celest. Mech. Dyn. Astron. **135**(32) (2023) <https://doi.org/10.1007/s10569-023-10134-7>
- [5] Aydin C.: *Exploration of vertical self-resonant bifurcations from DRO in the Earth–Moon CR3BP.* (2025) <https://arxiv.org/abs/2508.17286>
- [6] Aydin C., Batkin A.: *Studying network of symmetric periodic orbit families of the Hill problem via symplectic invariants.* Celest. Mech. Dyn. Astron. **137**(12) (2025) <https://doi.org/10.1007/s10569-025-10241-7>
- [7] Belbruno E.A.: *A new family of periodic orbits for the restricted problem.* Celestial Mechanics **25**, 195–217 (1981) <https://doi.org/10.1007/BF01230520>
- [8] Belbruno E.A.: *A new regularization of the restricted three-body problem and an application.* Celestial Mechanics **25**, 397–415 (1981) <https://doi.org/10.1007/BF01234179>
- [9] Bray T.A., Goudas C.L.: *Doubly Symmetric Orbits about the Collinear Lagrangian Points.* The Astronomical Journal **72**(2), 202–213 (1967)
- [10] Broucke R.A.: *Periodic orbits in the restricted three-body problem with Earth–Moon masses.* Tech. Rep. 32-1168, Jet Propulsion Laboratory (1968)
- [11] Bruno A.D.: *Simple periodic solutions of the restricted three-body problem in the Sun–Jupiter case.* In Russian, Institute of Applied Mathematics, Moscow, Preprint No. 66 (1993)
- [12] Bruno A.D.: *Zero-multiple and retrograde periodic solutions of the restricted three-body problem.* In Russian, Institute of Applied Mathematics, Moscow, Preprint No. 93 (1996)
- [13] Conley C. , Zehnder E.: *Morse-type index theory for flows and periodic solutions for Hamiltonian Equations.* Comm. Pure Appl. Math. **37**(2), 207–253 (1984) <https://doi.org/10.1002/cpa.3160370204>
- [14] Cors J.M., Garrido M.: *Symmetric comet-type periodic orbits in the elliptic three-dimensional restricted $(N+1)$ -body problem.* Physica D: Nonlinear Phenomena **470** (2024) <https://doi.org/10.1016/j.physd.2024.134426>

[15] Doedel E.J., Romanov V.A., Paffenroth R.C., Keller H.B., Dichmann D.J., Galán-Vioque J., Vanderbauwhede A.: *Elemental Periodic Orbits Associated with the Libration Points in the Circular Restricted 3-BODY Problem*. Internat. J. Bifur. Chaos **17**, 2625–2677 (2007) <https://doi.org/10.1142/S0218127407018671>

[16] Eliashberg Y., Givental A., Hofer H.: *Introduction to symplectic field theory*. GAFA 2000 (Tel Aviv, 1999) Geom. Funct. Anal., Special volume, Part II(2000), 560–673 https://doi.org/10.1007/978-3-0346-0425-3_4

[17] Feagin T.: *High-order explicit Runge-Kutta methods using m -symmetry*. Neural, Parallel, and Scientific Computations **20**, 437–458 (2012) <https://hdl.handle.net/10657.1/2296>

[18] Franz C.J., Russell R.P.: *Database of Planar and Three-Dimensional Periodic Orbits and Families Near the Moon*. J. Astronaut. Sci. **69**, 1573–1612 (2022) <https://doi.org/10.1007/s40295-022-00361-9>

[19] Ginzburg V. L.: *The Conley conjecture*. Ann. of Math. (2) **172**(2), 1127–1180 (2010)

[20] Hofer H., Wysocki K., Zehnder E.: *Finite Energy Foliations of Tight Three-Spheres and Hamiltonian Dynamics*. Ann. of Math. (2) **157**(1), 125–255 (2003) <https://doi.org/10.4007/annals.2003.157.125>

[21] Johnson S.K., Mortensen D.J., Chavez M.A., Woodland C.L.: *Gateway – a communications platform for lunar exploration*. IET Conference Proceedings (2022) <https://doi.org/10.1049/icip.2022.0544>

[22] Joung C., Koh D., van Koert O.: *Bifurcations of Highly Inclined Near Halo Orbits using Moser Regularization*. (2025) <https://arxiv.org/abs/2512.03849>

[23] Joung C., van Koert O.: *Computational symplectic topology and symmetric orbits in the restricted three-body problem*. Nonlinearity **38**(2) (2025) <https://doi.org/10.1088/1361-6544/ada7ba>

[24] Lamb J.S.W., Roberts J.A.G.: *Time-reversal symmetry in dynamical systems: A survey*. Physica D **112**, 1–39 (1998) [https://doi.org/10.1016/S0167-2789\(97\)00199-1](https://doi.org/10.1016/S0167-2789(97)00199-1)

[25] Lara M., Scheeres D.J.: *Stability Bounds for Three-Dimensional Motion Close to Asteroids*. J of Astronaut Sci **50**, 389–409 (2002) <https://doi.org/10.1007/BF03546245>

[26] Lee D.: *Conley-Zehnder Indices of Spatial Rotating Kepler Problem*. Journal of Topology and Analysis (2026) <https://doi.org/10.1142/S1793525326500238>

[27] Liu L., Hu C.: *Scheme design of the CHANG'E-5T1 extended mission*. Chinese Journal of Aeronautics **31**, 1559–1567 (2018) <https://doi.org/10.1016/j.cja.2018.04.012>

[28] Llibre J., Meyer K.R., Soler J.: *Bridges between the Generalized Sitnikov Family and the Lyapunov Family of Periodic Orbit*. J. Differential Equations **154**, 140–156 (1999) <https://doi.org/10.1006/jdeq.1998.3565>

[29] Llibre J., Roberto L.A.: *New doubly-symmetric families of comet-like periodic orbits in the spatial restricted $(N+1)$ -body problem*. Celest Mech Dyn Astr **104**, 307–318 (2009) <https://doi.org/10.1007/s10569-009-9213-6>

[30] Llibre J., Stoica C.: *Comet- and Hill-type periodic orbits in restricted $(N+1)$ -body problems*. Journal of Differential Equations **250**(3), 1747–1766 (2011) <https://doi.org/10.1016/j.jde.2010.08.005>

[31] Llibre J., Paşca D., Valls C.: *The circular restricted 4-body problem with three equal primaries in the collinear central configuration of the 3-body problem*. Celestial Mechanics and Dynamical Astronomy **133** (2021) <https://doi.org/10.1007/s10569-021-10052-6>

[32] McDuff D., Salamon D.: *Introduction to Symplectic Topology*. Oxford University Press, 3rd edition (2017)

[33] Meyer K.R.: *Periodic Solutions of the N-Body Problem*. Journal of Differential Equations **39**, 2–38 (1981)

[34] Meyer K.R.: *Periodic orbits near infinity in the restricted N-body problem*. Celestial Mechanics **23**, 69–81 (1981) <https://doi.org/10.1007/BF01228545>

[35] Meyer K.R.: *Comet like periodic orbits in the N-body problem*. Journal of Computational and Applied Mathematics **52**, 337–351 (1994) [https://doi.org/10.1016/0377-0427\(94\)90365-4](https://doi.org/10.1016/0377-0427(94)90365-4)

[36] Meyer K.R., Hall G.R., Offin D.: *Introduction to Hamiltonian Dynamical Systems and the N-Body Problem*. Second Edition. Springer (2009)

[37] Moreno A., Aydin C., van Koert O., Frauenfelder U., Koh D.: *Bifurcation Graphs for the CR3BP via Symplectic Methods*. J. Astronaut. Sci. **71**(51) (2024) <https://doi.org/10.1007/s40295-024-00462-7>

[38] Moulton F.R.: *A Class of Periodic Orbits of Superior Planets*. Transactions of the American Mathematical Society **13**(1), 96–108 (1912)

[39] Papadakis D.: *Families of three-dimensional periodic solutions in the circular restricted four-body problem*. Astrophys Space Sci **361** (2016) <https://doi.org/10.1007/s10509-016-2713-4>

[40] Poincaré H.: *Les méthodes nouvelles de la mécanique céleste*. Gauthier-Villars et Fils (1892)

[41] Robbin J., Salamon D.: *The Maslov index for paths*. Topology **32**(4), 827–844 (1993) [https://doi.org/10.1016/0040-9383\(93\)90052-W](https://doi.org/10.1016/0040-9383(93)90052-W)

[42] Robin I.A., Markellos V.V.: *Numerical determination of three-dimensional periodic orbits generated from vertical self-resonant satellite orbits*. Celest. Mech. **21**, 395–434 (1980) <https://doi.org/10.1007/BF01231276>

[43] Roy A.E.: *Orbital Motion*. Institute of Physics Publishing, Bristol and Philadelphia, 4th edition (2005)

[44] Siegel C.L., Moser J.K.: *Lectures on Celestial Mechanics*. Springer-Verlag Berlin Heidelberg (1995)

[45] Szebehely V.: *Theory of Orbits - The Restricted Problem of Three Bodies*. Academic Press, New York (1967)

[46] Williams J., Dawn T.F., Batcha A.L.: *A History of Orion Mission Design, Copernicus Software Development, and the Artemis I Trajectory*. AAS/AIAA Astrodynamics Specialist Conference, AAS 23-241 (2023)

[47] Zimovan-Spreen E.M., Howell K.C., Davis D.C.: *Near rectilinear halo orbits and nearby higher-period dynamical structures: orbital stability and resonance properties*. Celest. Mech. Dyn. Astron. **132**(28) (2020) <https://doi.org/10.1007/s10569-020-09968-2>

CENGİZ AYDIN

INSTITUT FÜR MATHEMATIK, UNIVERSITÄT HEIDELBERG, GERMANY

E-mail address: cengiz.aydin@hotmail.de